Metabolic Tumor Profiling with pH, Oxygen, and Glucose Chemosensors on a Quantum Dot Scaffold

Christopher M. Lemon[a], **Peter N. Curtin**[b], **Rebecca C. Somers**[b], **Andrew B. Greytak**[b,d], **Ryan M. Lanning**[c], **Rakesh K. Jain**[c], **Moungi G. Bawendi**[b], and **Daniel G. Nocera**[a,*]

[a]Department of Chemistry and Chemical Biology, Harvard University, 12 Oxford Street, Cambridge, MA 02138

[b]Department of Chemistry, Massachusetts Institute of Technology, 77 Massachusetts Avenue, Cambridge, MA 02139

[c]Edwin L. Steele Laboratory for Tumor Biology, Department of Radiation Oncology, Massachusetts General Hospital and Harvard Medical School, 100 Blossom Street, Cox-7, Boston, MA 02114

[d]Department of Chemistry and Biochemistry, University of South Carolina, Columbia, SC 29208

Synopsis

Acidity, hypoxia and glucose levels characterize the tumor microenvironment rendering pH, pO_2 and pGlucose, respectively, important indicators of tumor health. To this end, understanding how these parameters change can be a powerful tool for the development of novel and effective therapeutics. We have designed optical chemosensors that feature a quantum dot and an analyte-responsive dye. These non-invasive chemosensors permit pH, oxygen, and glucose to be monitored dynamically within the tumor microenvironment by using multiphoton imaging.

Introduction

Chemosensors have found application in the diverse areas of medicine,[1–6] national security,[7–13] aeronautics[14–22] and environmental science.[23–31] Signal transduction within a chemosensor construct involves the modulation of an output signal upon the recognition of an analyte by either a physical or chemical process[32–42] that is sometimes referred to as a "3R"—recognize, relay, and report—sensing scheme.[43,44] Of the various signal outputs, light emission is an especially convenient reporter of the presence of a target analyte. Modulation of emission lifetime, energy transfer efficiency, or intensity[45] is typically performed against a low background signal, and hence high dynamic ranges are achievable.[46] In addition, light emission can continuously report on analyte in real time[47,48] on nanometer length scales with a nanosecond time response.[49–51] Indeed, the presence of analyte has been detected at the single molecule limit by detecting emission.[52–57] Such sensors may be incorporated into a variety of imaging techniques including optical fibers and waveguides.[44,58–60] Together, these properties make luminescent chemosensors ideal for sensing, particularly for the detection of analytes in the biological milieu.

If luminescence is the desired signal transduction mechanism, then inorganic nanocrystals or quantum dots (QDs) are a preferred chemosensing scaffold owing to their unique photophysical properties.[61–74] Typically, the luminescence of suitably prepared QDs are unperturbed by changes in their environment (i.e. they are constant in both the presence and absence of an analyte),[75] affording a suitable framework for ratiometric sensing, which relies on signal changes relative to an internal standard to quantify the amount of analyte.

Sensor Design Principles

The salient feature of QD photophysical properties is tunability with particle size, which is due to quantum confinement. When a bulk semiconductor absorbs a photon with energy greater than the band gap, an electron is promoted from the valence band (VB) to the conduction band (CB), creating a free electron and free hole. If the photon has energy slightly less than the band gap by an amount equal to the phonon energy, an exciton will form. An exciton is a bound electron-hole pair that is held together by Coulombic interactions. The energy required to form an exciton is thus lowered by the binding energy of the electron and hole. For example, the exciton binding energy of CdSe is 15 meV or 1.4 kJ/mol. Excitons can move through the crystal lattice and transport energy, but not charge, as it is an electronically neutral entity.[76] As the size of the semiconductor decreases, the optical properties of the material are modulated. The relevant length scale of an exciton is its Bohr radius, which is defined as the spatial extension of the electron-hole pair. For CdSe, a photogenerated exciton delocalizes over a distance of ~12 nm. When the size of the semiconductor is on the order of the Bohr radius, the exciton wavefunction is perturbed, resulting in quantum confinement (Figure 1).[77,78] The energy of confinement of the exciton in the crystal exceeds the Coulomb energy, resulting in molecule-like states rather than bands in the bulk material. As a result, the exciton wavefunction is affected, giving rise to changes in the density of electronic states and the energy level separation. The exciton behaves as a particle in a box in which the energy depends on the size of the box ($\sim 1/r^2$).[79] Thus, the effective bandgap (E_g) increases with decreasing size and discrete energy levels arise at the band edges, thus resembling a molecular HOMO-LUMO gap.[61,78]

QDs have broad absorption profiles with high extinction coefficients that are complemented by narrow, Gaussian-shaped emission features that are tunable with size (vide supra). For CdSe QDs, small dots with a ~2 nm diameter exhibit blue emission under near UV excitation whereas larger dots with a ~6 nm diameter emit red light. Typically, QDs also exhibit high luminescence quantum yields; overcoating the QD with a higher band gap semiconductor (such as ZnS or CdZnS overcoats for CdSe) in a core/shell motif improves the emission quantum yield. The shell passivates sites on the surface of the core that would otherwise lead to nonradiative exciton recombination.[80,81] CdS-overcoated CdSe QDs can give a stable luminescence with near unity (>95%) quantum yields by sufficiently passivating the QD surface.[82] These properties contrast traditional organic fluorophores, which are prone to photobleaching as well as possessing narrow absorption profiles accompanied by broad emission features that tail into the red.[83] As a result, QDs have become popular fluorophores for biological imaging[84,85] and have found application as fluorescent tracers in microscopy,[86,87] imaging molecular targets,[88] cell tracking,[85,89] and tumor pathophysiology.[90]

If a chemosensor is to be coupled to a QD scaffold, then energy must be transferred between the QD and chemosensor active site. One of the most common methods of energy transfer within a nanoparticle QD construct is Förster resonance energy transfer or FRET.[91] In this mechanism, energy is transferred from a donor (D) fluorophore to an acceptor (A) molecule (Figure 2a) through-space via a long-range dipole-dipole interaction.[92] FRET decreases the emission intensity of the donor and transfers the energy to an acceptor molecule. Initially,

both the donor and acceptor have two electrons in their HOMO (i.e. a ground state singlet). Upon absorption of a photon, one of the electrons in the HOMO of the donor is promoted to the LUMO (Figure 2c). During FRET, the excited electron in the donor returns to the ground state without emitting a photon while, simultaneously, an electron in the acceptor is promoted from the HOMO to the LUMO (Figure 2c). The excited acceptor may then relax back down to the ground state either by fluorescence or by nonradiative decay.

In a FRET-based sensor, the donor is selected such that it has favorable absorption properties in the desired optical range while the acceptor is selected for analyte sensitivity and emission properties (i.e., optical readout of analyte concentration). The FRET pair must be judiciously selected such that the emission of the donor is energetically similar to the absorption of the acceptor so that efficient energy transfer can occur. The efficiency (E) of energy transfer between a donor and acceptor via FRET is reflected in donor-acceptor distances and energy transfer rates:

$$E = \frac{m k_{D-A}}{m k_{D-A} + \tau_D^{-1}} = \frac{m R_0^6}{m R_0^6 + r^6} = \frac{1}{1 + \frac{1}{m}\left(\frac{r}{R_0}\right)^6} \quad (1)$$

where r is the distance between the donor and acceptor, R_0 is the Förster distance or the distance at which the energy transfer efficiency is 50%, k_{D-A} is the rate of energy transfer, and τ_D is the lifetime of the donor in the absence of acceptor. If there are multiple acceptors per donor molecule, m accounts for the number of acceptors per donor. Based on Eq. 1, it is clear that E increases with increasing values of m. With an increase in E, the amount of output signal from the acceptor is increased; this is particularly advantageous for imaging and sensing applications. Thus, the majority of QD sensor constructs feature many acceptor fluorophores per QD donor (vide infra). It should be noted that for systems where $m > 1$, measurements of r are average distances that reflect the ensemble of donor-acceptor constructs, unless each construct has identical fixed donor-acceptor distances and identical values of m. The FRET efficiency E can be determined experimentally with knowledge of emission lifetimes,

$$E = 1 - \frac{\tau_{D-A}}{\tau_D} \quad (2)$$

where τ_{D-A} is the lifetime of the donor in the presence of acceptor. The Förster distance (R_0) can be calculated from the spectral overlap integral of donor emission and acceptor absorption (Figure 2b):

$$R_0^6 = \frac{9000\,(\ln 10)\kappa^2 \Phi_D}{128\,\pi^5 N n^4} \int_0^\infty F_D(\lambda)\varepsilon_A(\lambda)\lambda^4 d\lambda \quad (3)$$

where $F_D(\lambda)$ is the normalized emission intensity of the donor, $\varepsilon_A(\lambda)$ is the extinction coefficient of the acceptor at wavelength λ, κ^2 is the relative orientation factor of the transition dipoles, Φ_D is the quantum efficiency of the donor, N is Avogadro's number and n is the index of refraction of the medium. The latter half of the equation is known as the spectral overlap integral and is often denoted by the variable J. Typically, critical FRET length scales for R_0 range from 2–9 nm.[46] Because QDs have readily tunable emission profiles, they serve as attractive FRET donors because the overlap integral in Eq. 3 may be adjusted with fidelity.

FRET may occur by one- or two-photon absorption. The latter is especially important for *in vivo* applications because absorption of endogenous chromophores, particularly hemoglobin

and melanin, is minimal in the so-called "tissue transparency window" of 600–1100 nm. Moreover, owing to the decrease of scattering with increasing wavelength, the penetration depth of these wavelengths is on the order of millimeters in most tissues.[93] A further advantage of two-photon excitation is shown in Figure 3, which shows a sample of fluorescein irradiated under (a) one- and (b) two- photon excitation conditions. Under single photon excitation, the focal region is proportional to the intensity of the incident light. Conversely, the excitation profile depends on the square of the intensity for a two-photon process, and rapidly decays from the focal point. As a result, the two-photon excitation volume is much smaller than a one-photon excitation volume, thereby increasing the spatial resolution of the signal. Indeed, the two-photon excitation densities are factors of 10^2 and 10^4 smaller at the axial distances of 1.1 and 10 µm, respectively, from the focal point resulting in an excitation volume element that is substantially smaller than that of a one-photon excitation.[94] For these reasons, the observed emission under one-photon excitation exhibits an hour-glass shape, generating a streak of emission along the beam path. In contrast, the two-photon excitation exhibits a sharp pinpoint emission at the focal point of the excitation source. As a result, the small focal volume of two-photon excitation minimizes photobleaching and photodamage and is especially convenient for producing spatial maps of an analyte in heterogeneous microenvironments.[95–97] For these reasons, multiphoton laser scanning microscopy (MPLSM) has become a powerful, routine imaging technique. It uses NIR light in the 600–1100 nm region to exploit the tissue transparency window and allow for greater depth penetration and deep tissue imaging. MPLSM provides noninvasive three-dimensional optical imaging with significant depth penetration (450–600 µm) and approximately 1 µm of spatial resolution.[93,98–101]

The two-photon transition occurs via a virtual state. The absorption cross-section (σ_2) can be estimated using a single intermediate state approximation,[102]

$$\sigma_2 = \sigma_{ij} \, \sigma_{jf} \, \tau_j \quad (4)$$

where σ_{ij} is the absorption cross-section for the transition from the initial state i to the intermediate state j, σ_{if} is the absorption cross-section for the transition from the intermediate state j to the final state f and τ_j is the lifetime of the intermediate state. The parameter τ_j determines the time scale for photon coincidence and is 10^{-15} s or less for a virtual state (i.e., simultaneous photon absorption). Alternatively, multiphoton excitation may be sequential if the intermediate state is a real state with a lifetime of 10^{-9} to 10^{-12} s. A one-photon absorption cross-section (σ_1) may be estimated using the length of the transition dipole. For a typical organic fluorophore with a 10^{-8} cm dipole transition, σ_1 is approximately 10^{-16} or 10^{-17} cm^2. Using these values and Eq. 4, one may estimate a two-photon absorption cross-section of 10^{-49} cm^4 s/photon or 10 Göppert-Mayer (GM) for a typical chromophore, where 1 GM = 10^{-50} cm^4 s/photon.[103] Indeed, the two-photon absorption cross-section of typical fluorophores is 10–100 GM.[103–106] For example, fluorescein, a popular fluorescent dye commonly used in biological labeling, exhibits σ_2 from 8 GM to 37 GM in the 690–960 nm range, with the absorption maximum observed at 780 nm.[105] Some conventional fluorophores exhibit notably high σ_2 values: Cy3 with 140 GM and Rhodamine 6G with 150 GM, both at 700 nm.[105] More recently, design principles have been recognized that have led to the preparation of organic molecules with large (1000–10,000 GM) two-photon absorption cross-sections.[94,107] Owing to low two-photon absorption cross-sections of typical dyes, most analyte-sensitive dyes cannot be used directly for MPLSM applications. Conversely, QDs exhibit large two-photon absorption cross-sections,[108–112] with values of σ_2 as high as 47,000 GM for CdSe/ZnS QDs.[109] This exceptionally high σ_2 gives rise to the utility of the QD as a two-photon antenna for an

analyte-sensitive dye so that biological sensing can be accomplished under multiphoton excitation.

To that end, our research groups have developed a series of ratiometric, two-photon optical sensors where the QD is a scaffold to which an analyte sensitive fluorophore is appended. The QD serves as a (multi)photon antenna and absorbed energy is transferred to the attached dye via FRET. By having a two-color response (i.e., QD and appended fluorophore with different emission profiles), one can internally reference the output intensity of the construct, making ratiometric sensing possible. If QD emission is constant in a given construct, one can use the fluorophore:QD emission ratio to quantify analyte concentration. This is usually the case, and applies in the chemosensors that we have constructed. If both donor and acceptor emission profiles change as a function of analyte, the fluorophore:construct (QD + fluorophore) emission ratio serves as a measure of analyte concentration. This is a self-consistent measurement that is independent of construct concentration and environmental factors (sample scattering, turbidity, etc.), rendering this sensing strategy particularly useful for biological applications. Figure 4 illustrates the different optical responses that we have exploited. In a "turn-on" sensor (Figure 4a), fluorophore emission is enhanced upon analyte binding. This strategy is used in glucose binding to boronic acid modified fluorophores. In a "turn-off" sensor (Figure 4b), dye emission is quenched in the presence of analyte. By using phosphorescent molecules, we have developed oxygen sensors that operate by collisional quenching. Finally, changes in FRET efficiency have been used to measure analyte concentration. The spectral overlap of the QD and fluorophore can be modulated as a function of analyte (Figure 4c). Alternatively, varying the QD-fluorophore distance with analyte concentration can modulate the FRET efficiency (Figure 4d). Both of these strategies have been used in the development of pH sensors. These various sensing motifs are described below.

Tumors as a Chemosensing Target

New chemosensors and probes for tumor biology can answer fundamental questions about cancer development and disease progression.[113] There are three key parameters that serve to define the metabolic profile of a tumor: glucose, pH, and oxygen, as these serve as direct measures of tumor consumption, metabolism, and respiration, respectively.[114,115] Due to the biological relevance of these three analytes, the scope of this manuscript is limited to QD-based sensors for pH, O_2, and glucose. Other examples will be included where relevant. The interested reader is directed to a series of reviews by Mattoussi and co-workers covering additional applications of QDs to the fields of biosensing and bioimaging.[84,116–118]

While most normal cells rely on mitochondrial oxidative phosphorylation, tumors exploit anaerobic glycolysis for energy needs.[119,120] Since glycolysis is less efficient than mitochondrial respiration, tumors exhibit greater glucose consumption than normal tissue. As a result, the tumor environment is characterized by low extracellular pH (6.6–6.8)[115] due to the presence of lactic acid[121] as a product of anaerobic glycolysis and carbonic acid, which is derived from dissolved CO_2 as a product of aerobic respiration; these species tend to accumulate in the tumor due to inefficient removal pathways.[122]

Tumor vasculature is heterogeneous, dilated and leaky, resulting in inefficient delivery of blood and oxygen.[123,124] As a result, the tumor is characterized by hypoxia (pO_2 5 torr), which stimulates angiogenesis (the formation of new blood vessels), can induce tumor cell apoptosis (programmed cell death), and select for tumor cells with defects in apoptosis pathways. The concentration of pH and oxygen species affects tumor cell metabolism, tumor cell proliferation and viability, and glucose and oxygen consumption rates.[115] Together, tumor acidity and hypoxia incapacitate immune cells, render tumor cells invasive and

metastatic, and induce the expression of angiogeneic factors, which trigger and stimulate tumor growth.[125–127]

One emerging strategy to treat cancer is to target angiogenesis, as tumors require blood vessels for growth and metastasis.[128–133] More than 500 million people worldwide are predicted to benefit from pro- or anti-angiogenesis treatments.[134] While anti-angiogeneic therapy has provided short-term benefits,[135,136] long-term studies show that the tumors reappear more aggressively,[137–139] possibly because antiangiogenic agents increase the population of cancer stem cells (CSCs) in a tumor by generating a hypoxic environment.[140] CSCs are slow-cycling cells that exhibit a metastatic phenotype. They can give rise to diverse populations of cells, including nontumorigenic cancer cells and stromal cell; thus, they are implicated in tumor repopulation and subsequent relapse after chemotherapy.[141–147] Additionally, hypoxia induces the expression of stem cell markers in cancer cells[148,149] and antiangiogenic therapy elicits malignant progression of tumors.[150] As angiogenesis allows tumors to grow in size, their leaky vasculature results in hypoxia that fuels the CSC population.[151] For these reasons, a *combination* of antiangiogeneic therapy and chemotherapy has been shown to be effective in the long term.[152] However, this combination of therapies raises a paradox: chemotherapy attacks malignant tissue directly while anti-angiogeneic therapy destroys the very vessels required to deliver drugs. Thus, one might expect that antiangiogeneic therapy may hinder the efficacy of chemotherapeutics.[153–155]

One of us has hypothesized that certain antiangiogenic therapies can transiently "normalize" the distended tumor vasculature, resulting in the more efficient delivery of oxygen and drugs.[113] In this "Normalization Hypothesis," there is a time window in which tumor vasculature resembles normal vessels after the administration of an antiangiogenic drug. Since the normal tissue is less leaky and dilated, the transport of nutrients, waste, oxygen, and drugs is greatly enhanced. However, excessive dosage of anti-angiogenic drugs results in the destruction of vessels, making them inadequate to deliver drugs. Such therapies improve tumor oxygenation over brief periods of time, thereby suggesting the presence of a vasculature normalization window.[136,156] However, the functional parameters of glucose concentration, pH, and pO_2 have not been efficiently characterized as this process occurs. By profiling the metabolism of the tumor through monitoring these species, tumor health may be assessed and therefore chemotherapeutics can be timed appropriately to have a maximal effect. In this way, understanding how the metabolic profile of the tumor changes as a function of disease progression provides a path to develop novel therapeutics based on antiangiogenic agents.

To this end, the need to monitor real time changes in pH, pO_2 and glucose concentrations in the tumor microenvironment provides an imperative for the creation of QD nanosensors. Ideally, one could monitor the normalization process by monitoring how the oxygen and pH levels change over the course of antiangiogenic therapy. Once these functional parameters of the tumor resemble that of normal tissue, the tumor could then be treated with a high dose of chemotherapy or radiation, as the circulation of drugs and oxygen would be most efficient to destroy the tumor. Conversely, oxygen levels must be monitored such that antiangiogenic therapies are not overdosed to excessively prune the vasculature. This may leave behind viable CSCs to repopulate the tumor. Alternatively, such oxygen sensors could be used to determine the oxygen level in a tumor (anoxic, hypoxic, or normoxic) so that an appropriate course of therapy could be administered given the tumor type, thus resulting in "personalized medicine." For example, radiation therapy relies on high oxygen content to produce and propagate reactive oxygen species to destroy tumor cells,[157] but hypoxic tumors are much less sensitive to radiation.[123] The ability to rapidly determine and monitor

changes in tumor oxygenation, pH, or glucose can therefore help determine the best course of therapy and improve patient outcomes.

Quantum Dot Conjugation Chemistry

As synthesized, QDs are hydrophobic with tri-*n*-octylphosphine oxide (TOPO) or some other hydrophobic molecule as the capping ligand.[61] The surface of the QD must be modified to impart water solubility and biocompatibility. One method to confer water solubility is to coat a CdSe/CdS or CdSe/ZnS core/shell structure with a layer of silica,[158] while another is to use mercaptoacetic acid to passivate the surface.[159] The surfaces of QDs have been modified with phospholipids,[86] amphipilic polymers,[88,160] dendrimers,[161–166] and oligomeric phosphines[167] to make them water-soluble. An alternative approach is to exchange the hydrophobic capping ligand for a multidentate hydrophilic ligand.[89,168–171] We have developed two such ligands to solubilize QDs: a dihydrolipoic acid-polyethylene glycol (DHLA-PEG) polymer[172] and an imidazole-based copolymer.[173] Schematic representations of these two ligand systems are presented in Figure 5. It should be noted that Mattoussi and co-workers reported a seminal contribution for a similar set of functionalized DHLA-PEG ligands.[174–176] While DHLA is commonly used to solubilize QDs in aqueous environments, these QDs are unstable below pH 6, are not easily derivitized, and typically show high nonspecific binding in cell cultures. The stability of the QDs is greatly enhanced by addition of a PEG unit in the DHLA-PEG ligand. These QDs are stable from pH 5.0 to 9.5, have a small a small hydrodynamic diameter (10–12 nm), and preserve a high quantum yield ($\Phi = 65\%$ in hexane and $\Phi = 30$–40% in water after ligand exchange). Additionally, the terminal hydroxyl group of the DHLA-PEG ligand enables further derivitization to either a terminal amine or carboxylic acid. This allows the surface charge to be tuned as well as permit conjugation of fluorescent tags, proteins, or other molecules of interest. QDs solubilized with a 4:1 blend of DHLA-PEG and the amine-functionalized analog (Figure 5a) showed minimal nonspecific binding to HeLa cell cultures. Moreover, specific targeting of cells was achieved. COS7 cells transfected with human EGF receptor were incubated with biotinylated EGF. DHLA-PEG QDs that were modified with streptavidin selectively bound to the biotinylated cells, thus demonstrating proof-of-concept specific cell tagging *in vitro*.[172]

The DHLA-PEG QDs are not exceptionally stable over long periods of time. After one week of storage at 4 °C in the dark, the QD exhibited ligand loss, as evidenced by electrophoresis studies, and an increase in nonspecific binding to HeLa cells *in vitro* was observed. To overcome this deficiency, a polymeric imidazole ligand (PIL) was developed (Figure 5b).[173] This copolymer is prepared by reversible addition-fragmentation chain transfer (RAFT) polymerization[177] of three vinyl-modified monomers: ~50% imidazole for QD surface binding, ~25% PEG for water solubility, and ~25% terminal amine for further derivitization. The resultant polymer has a typical molecular weight of ~14 kDa with a very narrow distribution (PDI < 1.2). QDs coated with this ligand are photostable under ambient conditions for at least 2 months, whereas the DHLA-PEG QDs precipitate within 15 hours. Additionally, these modified QDs are stable from pH 5.0 to 10.5, have a small hydrodynamic diameter (10–12 nm), and exhibit high quantum yields ($\Phi = 90\%$ in octane and $\Phi = 65\%$ in water after ligand exchange). Together, these properties make PILs attractive ligands for biological applications. Specific binding between streptavidin-modified PIL QDs and HeLa cells transfected to express biotin on the cell surface was observed. If the PIL polymer contains < 10% free amine, little nonspecific binding to HeLa cells is observed. Moreover, PIL-coated QDs exhibited negligible nonspecific binding to serum proteins, making them attractive fluorophores for *in vivo* applications.

The distribution dynamics of PIL QDs was studied in the tumor vasculature of live mice implanted with a breast tumor model. QD tracking was performed using MPLSM with 880 nm excitation and the results are illustrated in Figure 6; red signal is due to QD emission while green signal is due to green fluorescence protein (GFP) expression in the vessel wall. Immediately after injection, it was found that QDs were confined to the vessel lumen. After 3 hours, the QDs have begun to clear from the vasculature and diffuse into the tumor tissue. After 6 hours, the QDs have extravasated into the tumor tissue, giving a uniform distribution of red signal over the field of view. This result indicates that PIL-coated QDs are small, stable, and biocompatible, rendering them useful scaffolds to construct sensors for *in vivo* applications.[173]

We devised a QD nanoparticle size series (10–150 nm) with the aim of understanding the dynamics of QD extravasation and probe transport barriers in tumor vasculature.[178] Small (10–20 nm) particles were solubilized using PIL,[173] whereas medium (20–70 nm) particles were coated with a layer of silica. Large (100–150 nm) particles were prepared using preformed silica particles as templates to incorporate amine-functionalized QDs via electrostatic interactions. To study biological transport, a mixture of three nanoparticles (12 nm particles with 476 nm emission, 60 nm particles with 606 nm emission, and 125 nm particles with 540 nm emission) was injected into a mouse bearing an Mu89 human melanoma xenograft. The tumor was imaged using MPLSM with 800 nm excitation. After an extravasation period of 90 minutes, the distribution of the particles was recorded. It was found that the 12 nm particles readily diffuse away from the vessels and into the tumor tissue with minimal hindrance. Conversely, the 60 nm particles remain in the perivasculature region of the tumor ($< 10 \mu m$ from the vessel) while the 125 nm particles do not appreciably extravasate.[178]

QD-Based pH Chemosensors

The earliest and most prevalent QD chemosensors of pH featured a change in fluorescence intensity and/or wavelength as a function of pH. The chemosensors usually use CdTe QDs, either as a suspension[179–186] or in layered polymer/QD hybrid microspheres.[187–191] Other QD examples including CdSe/ZnS core-shell structures,[192,193] graphene QDs,[194] and Mn-doped ZnSe QDs[195] have also exhibited a pH response. Of these systems, few are ratiometric as there is no internal intensity standard, though some feature multicolor emission with the inclusion of a second QD and the emission ratio varies as a function of pH.[181,189,190,192] The proton flux of ATP synthase in viruses[181,182] and pH changes in human ovarian cancer cells[193] have been monitored using this type of QD chemosensor. Alternatively, a variety of QDs have been coated with a pH-responsive polymer. In terms of synthetic polymers, diblock copolymers of pyridine and pyrene[196] or benzene[197] are pH-sensitive; the former example is ratiometric and operates using FRET. QDs have also been coated with non-fluorescent biopolymers such as the polysaccharide chitosan[198,199] or human serum albumin;[200] conformational changes of these polymers are responsive to pH and thus modulate QD fluorescence. Additionally, QDs have been combined with a chaperonin protein template in a solid-state electrochemical pH sensor.[201]

A more popular methodology for pH sensing appends a fluorophore with a known pH response profile to a QD scaffold. To this end, pH-sensitive proteins, such as the fluorescent protein mOrange, have been appended to QDs to furnish FRET-based ratiometric pH sensors.[202,203] For solution-based sensors, a variety of pH-responsive chromophores have been used: 4-nitrophenylazo-phenolate,[204,205] dopamine,[206,207] fluorescein derivatives,[208–210] and carbocyanine dyes.[211] Also, a variety of solid-state devices comprised of sol-gel matrices combine a QD with bromocresol purple,[212] Nile Blue,[213] and a variety of other pH dyes.[214]

We have elaborated a FRET-based chemosensing scheme to produce a series of ratiometric pH sensors. Amide bond formation was used to covalently append a squaraine dye ($pK_a \sim$ 8.5) to a CdSe/ZnS QD solubilized with an amphiphilic polymer, giving a dye:QD ratio of ~ 3:1. This construct operates via a modulation of the FRET efficiency as a function of pH (Figure 4c). While the QD emission is pH independent, the absorbance of the squaraine dye increases with decreasing pH, thereby changing the spectral overlap integral J (Eq. 3) as a function of pH. Under basic conditions (pH 10), the absorbance of the squaraine is suppressed, R_0 is ~6.0 nm, and the emission spectrum of the sensor is dominated by the QD. Under acidic conditions (pH 6), the absorbance of the squaraine is at a maximum and R_0 is ~6.8 nm. Because the FRET efficiency has increased, QD emission is quenched and emission from the dye dominates. Thus, the ratio of QD to squaraine emission serves as a measure of pH. This ratiometric approach is powerful, enabling the use of the sensor in turbid media. When the sensor was used in a suspension of silica microspheres, the sensitivity of the sensor was preserved, making this an attractive construct for biological microenvironments displaying heterogeneity.[215]

To better match the biologically relevant pH regime of 6–8, a SNARF-5F fluorophore (pK_a ~ 7.2) was employed as a pH chemosensor.[216] The construct uses a CdSe/CdZnS QD coated with a dihydrolipoic acid-modified poly(amino amine) (DHLA-PAMAM) dendrimer for water solubility. The starburst structure provides a high degree of ligation to couple many dyes per QD; dye:QD ratios of 26:1 may be obtained. Similar to the squaraine sensor, the SNARF-5F sensor operates by modulating the spectral overlap integral as a function of pH. It was found that R_0 increased from 4.46 nm to 4.68 nm upon increasing the pH from 6 to 9; this corresponds to FRET efficiencies of 25% and 37.5%, respectively. The QD emission dominates at low pH while SNARF-5F emission dominates at high pH, owing to quenched QD emission. The construct was studied in phosphate buffer with 4% BSA under 365 nm excitation. The sensor exhibits excellent sensitivity in the 6 to 8 pH range, although SNARF-5F fluorescence is diminished relative to the construct in the absence of BSA. The ratiometric pH-dependent emission profile is maintained under two-photon excitation (λ_{exc} = 800 nm) of the QD chemosensor.

Preliminary *in vivo* imaging studies using the QD-SNARF-5F chemosensor have been performed. Mice bearing a chronic dorsal skinfold chamber were implanted with LS174T human colorectal adenocarcinoma xenografts. A solution of the sensor was applied directly to the tumor and allowed to diffuse into the tissue. Cascade blue dextran was co-injected as a vascular marker. MPLSM was performed using 800 nm excitation and fluorescence was collected in three separate optical channels: blue for vascular imaging, green for QD emission, and red for SNARF-5F emission. Figure 7 shows a series of *in vivo* images of the tumor; additional images are provided in Figure S1. Figure 7a illustrates the hallmarks of tumor vasculature (blue)–dilated, heterogeneous vessels that do not uniformly penetrate in the tissue. A radial pH gradient emanating from the vessel is observed, as the red signal transitions to green from left to right across the image. It is likely that the large vessel provides sufficient clearance of metabolic byproducts to maintain near-normal pH whereas the tissue far from the vessel accumulates lactic acid from glycolysis. Figure 7b features a network of vessels in the tumor tissue, which is rather acidic as evidenced by the dominating green signal on either side of the vascular network that runs through the center of the image. Figure 7c clearly illustrates a pH gradient in the tumor tissue as evidenced by the transition from red to green signal, thereby demonstrating the microheterogeneity of the tumor environment.

The ratio of red to red+green emission (SNARF:construct ratio) was used to measure the pH, as QD emission is not constant as a function of pH, due to changes in FRET efficiency. A qualitative proof-of-concept experiment was performed in which glucose was injected and

images were acquired over 90 minutes following injection. As expected, the red:(red+green) ratio decreased over this time, as the pH should decrease after inducing hyperglycemia (i.e., the average QD emission increases as SNARF-5F emission decreases). However, many of the observed ratios fell outside of the values obtained from *in vitro* calibration. As a result, we have demonstrated qualitative pH changes *in vivo*. To obtain quantitative results, additional calibrations must be performed that better mimic *in vivo* conditions, such as *ex vivo* tissue calibrations. One additional issue that complicates the use of the ratio is that red and green light scatter differently in tissue.[217] As a result, ratios will depend on both the depth of imaging as well as the optical properties of the tissue above the imaging plane.

As an alternative to using a pH-responsive fluorophore, we have developed a pH sensor that operates by conformational control of FRET;[218] sensing is accomplished by physically modulating the donor-acceptor distance as a function of analyte concentration (Figure 4d). In this construct a PIL-coated CdSe/CdS QD is appended with Rox, a pH-insensitive fluorophore. The two are connected with a cytosine-rich oligonucleotide that folds or unfolds in response to pH changes due to protonation or deprotonation of the cytosine imino group. At high pH (~8), the oligonucleotide adopts an extended duplex structure, separating the QD and Rox dye by 9.4 nm. As a result FRET efficiency is low (9%) and QD emission dominates. Conversely, the protonated oligonucleotide (pH 6) adopts a folded triplex motif, reducing the QD–Rox distance to 6.3 nm, which corresponds to a 48% FRET efficiency. At low pH, Rox emission is greatly enhanced and QD emission is quenched, providing a ratiometric pH response. The effective pK_a for this duplex/triplex transition is ideal for studying mildly acidic biological environments. HeLa cells were incubated with the QD-Rox sensor for 10 minutes, enabling the sensor to be endocytosed. The cells were then imaged using confocal microscopy (λ_{exc} = 488 nm) and the pH of the resultant endosomes was determined 0, 10, 20, and 30 minutes after incubation. During this time, the pH decreased from an average value of 7.4 to 6.9, with a significant number of endosomes exhibiting a pH of 6.0 after 30 minutes demonstrating the utility of this construct in biologically relevant pH regimes.

QD-Based Oxygen Chemosensors

Many oxygen-responsive phosphors have been reported based on iridium[219] or ruthenium[220] polypyridine complexes. Platinum and palladium porphyrins are especially well-suited for O_2 sensing applications, as well, due to their strong room temperature phosphorescence in the 650–800 nm range and long (~10^2 μs) phosphorescence lifetime.[221] Most oxygen chemosensors heretofore have relied on the immobilization of these porphyrins in polymer matrices,[221,222] on solid surfaces,[221,,223] or in mesoporous silica.[221,224] To date, there have been very few examples of QDs paired with an O_2-responsive phosphor and nearly all have been embedded in a sol-gel matrix. These solid state sensors have featured Ru(II) bipyridine (bpy) complexes,[225,226] Ru(II) phenanthroline (phen) complexes,[226] Pt(II) porphyrins,[227–229] and Pt(II) octaethylporphyrin ketone.[230,231] Only the Pt(II) octaethylporphyrin ketone examples utilize the QD as a FRET donor to excite the phosphor; in the other examples, the QD merely serves as an internal intensity standard for ratiometric sensing.

In addition to our work, there is one QD-based O_2 sensor for solution sensing applications. In this construct, an imidazole-modified pyrene molecule was surface bound to a QD and served as the phosphor the sensor used FRET for signal transduction.[232] We paired a ZnSe/CdSe/CdZnS core/shell/shell motif QD with an Os(II)(bpy) or Os(II)(phen) complex as the oxygen-responsive phosphor.[233] The QDs were solublilzed in water using *n*-octylamine-functionalized poly(acrylic acid), which features terminal carboxylic acids for coupling amine-functionalized Os(II) complexes. Due to the high number of surface carboxylates, the

sensor features either 135 Os(II)(phen) or 57 Os(II)(bpy) complexes per QD. Oxygen is detected by collisional quenching of the triplet metal-to-ligand charge transfer (MLCT) band of the Os(II) complex with molecular oxygen (a ground state triplet) in a "turn-off" sensing scheme (Figure 4b). Quenching of the excited state follows Stern-Volmer kinetics:[234]

$$\frac{\tau_o}{\tau}=1+k_q\tau_o[O_2] \quad (5)$$

where τ_o is the natural radiative lifetime of the phosphor, τ is the lifetime of the phosphor at a given oxygen concentration or $[O_2]$, and k_q is the bimolecular quenching rate constant. The emission spectra of these chemosensors exhibit features from the QD and the ^{3}MLCT of the Os(II) complex. In the covalent construct, QD emission is attenuated while Os(II) complex emission is enhanced relative to the free components, indicative of a FRET interaction. Indeed, the quantum yield of the ^{3}MLCT band is increased in the construct while the lifetime of the QD decreases. FRET calculations indicate a 67% FRET efficiency ($R_0 = 3.4$ nm) for Os(II)(byp) and a 50% FRET efficiency ($R_0 = 4.0$ nm) for Os(II)(phen). Since the QD serves as a two-photon antenna, the sensor displays a dramatic enhancement of the ^{3}MLCT emission under two-photon irradiation ($\lambda_{ex} = 920$ nm); emission is nearly undetectable for the free Os(II) complex under direct two-photon excitation. In terms of the oxygen sensitivity, ^{3}MLCT emission is quenched by ~20% in the presence of 1 atm O_2 while the QD emission is unaffected. This establishes a ratiometric sensing profile in which the O_2 concentration can be determined by taking the QD:Os(II) emission ratio. To further quantify the oxygen sensitivity of the sensor, the Os(II)(phen) construct was studied over an O_2 pressure range of 0–760 torr. The sensor displays Stern-Volmer quenching kinetics with $k_q = 1.8 \times 10^9$ M^{-1} s^{-1} or 3000 $torr^{-1}$ s^{-1}.

The Os(II)-based constructs lack sensitivity in the biologically-relevant 0–160 torr range. To overcome this limitation, we have utilized Pd(II) porphyrin complexes as the phosphor.[235] As alternative to covalent strategies, we sought to exploit the surface chemistry of QDs and use supramolecular assembly as a means of conjugate formation. To this end, a series of Pd(II) porphyrins with *meso* pyridyl substituents were prepared; this functionality enables the phosphor to coordinate directly onto the surface of the QD. Titration experiments reveal that porphyrins with two pyridyl substituents in a *cis* motif bind most efficiently ($K_A \sim 10^7$ M) to the QD, as these compounds act as bidentate ligands on the QD surface. Upon surface binding, QD emission is quenched with a concomitant enhancement of porphyrin emission (both excited state lifetime and quantum yield). It was found that these sensors display remarkably high FRET efficiencies (94% with $R_0 = 4.1$ nm) due to judicious selection of QD donor to maximize spectral overlap. As with the Os(II)-based sensors, emission of the construct under two-photon irradiation ($\lambda_{exc} = 800$ nm) is substantial whereas it is undetectable for the Pd(II) porphyrin alone. In terms of oxygen sensitivity, porphyrin emission in the construct is quenched significantly under ambient air whereas the emission intensity is ~ 10^2 times greater in the absence of oxygen. Since QD emission is unaffected, the conjugate exhibits a ratiometric O_2-sensing profile.

While this system has been fully characterized in organic solvents, a method of translating this system to an aqueous environment was sought. To this end, we encapsulated the preformed QD-porphyrin assemblies in a phospholipid micelle. Qualitatively, the micelles display similar photophysical properties and oxygen sensitivity as their organic-soluble congeners. With a water-soluble sensor, the oxygen quenching kinetics were studied in much greater detail. Oxygen-dependent emission spectra were fit to a two-component kinetics model, giving $k_q = 1.2 \times 10^9$ M^{-1} s^{-1} for the dominant (~85%) component of the fit. This model was substantiated with oxygen-dependent lifetime measurements of the sensor. Lifetime data was fit to a biexponential decay with the long component obeying normal

Stern-Volmer kinetics (Eq. 5) with $k_q = 1.0 \times 10^9$ M^{-1} s^{-1} while the short component exhibits a quenching sphere of action, giving an exponential O$_2$-dependence, with $k_q = 4.5 \times 10^8$ M^{-1} s^{-1}. Based on this data, we propose that the Pd(II) porphyrin resides in two distinct environments in the micelle: (1) dispersed in the hydrophobic "solvent" of the QD ligand and the oleate groups of the micelle (displaying normal Stern-Volmer kinetics); and (2) bound on the surface of the QD (exhibiting quenching sphere of action kinetics due to modified accessibility to the quencher). The chemosensor was studied at 37 °C to determine the quenching parameters for calibrating *in vivo* measurements. The long lifetime component gave a $k_q = 1.7 \times 10^9$ M^{-1} s^{-1} at 37 °C.

In vivo imaging and lifetime-based oxygen measurements were made by systemically injecting mice bearing chronic dorsal skinfold chambers or cranial windows. Vascular imaging was performed using MPLSM with 850 nm excitation and emission light was collected in three separate optical channels: green for QD emission, yellow for autofluorescence, and red for porphyrin emission. The signal of the green channel is well dispersed while the red channel is quite variable, qualitatively indicating differences vessel oxygenation (i.e. arteries vs. veins). Figure 8 illustrates the homogenous distribution of the green (QD emission) signal for two locations in a cranial window model. A movie of Figure 8a that illustrates the steps through the vasculature in three-dimensions is provided as the Supporting Information. Qualitative differences in the intensity of the red channel were observed to differentiate arteries from veins. Lifetime-based measurements allowed *in vivo* oxygen levels to be quantified. The ratio of the red to green channels provides a ratiometric response as the green channel is invariant to O$_2$. However, differences in the scatter of red and green photons complicate the use of *in vivo* intensity as a quantitative measure of O$_2$. For this reason, lifetime measurements are more easily exploited to calibrate ratios at a given depth.

QD-Based Glucose Chemosensors

The use of glucose oxidase is a well-established method for quantifying glucose concentrations using a colorimetric assay.[236,237] As a result, many QD-based glucose sensors feature glucose oxidase appended to a QD surface as soluble optical sensors,[238–244] solid state optical sensors,[245–247] or solid state (photo)electro-chemical/electrochemiluminescent sensors.[248–254] In these sensors, H$_2$O$_2$, which is generated during enzyme turnover, quenches QD luminescence in optical sensors, or is detected electrochemically to quantify the amount of glucose in the sample. Other enzymatic QD-based glucose sensors use glucose dehydrogenase[255] or a combination of glucose oxidase and horseradish peroxidase[256–258] to subsequently manage the generated H$_2$O$_2$. In a related approach, the generated H$_2$O$_2$ has been used to reduce AuCl$_4^-$ to Au, resulting in the "biocatalytic growth" of Au nanoparticles, which modulate QD luminescence.[259]

QD-based enzymatic glucose chemosensors complement the earlier work of Mattoussi, Mauro, and co-workers.[260] In these systems, maltose binding protein (MPB) is bound to the surface of a QD using a polyhistidine tag. The sugar binding pocket of MPB is blocked with β-cyclodextrin modified QSY-9, resulting in FRET quenching of QD emission. In the presence of maltose, the QSY-9 dye is displaced and QD emission is observed. An alternative construct features Cy3-labeled MPB bound to the QD surface. The Cy3 fluorophore serves as a bridging donor and acceptor, the emission of which ultimately serves to signal the presence of analyte. The sugar binding pocket of Cy3-MPB is blocked with β-cyclodextrin modified Cy3.5. In the absence of maltose, FRET quenching of Cy3 occurs and only Cy3.5 emission is observed. When maltose is present, the Cy3.5 dye is displaced and Cy3 is rendered emissive.

In terms of non-enzymatic glucose sensing, FRET-based sensors have exploited the assembly of two QDs with different emission wavelengths[261] or a QD and a Au nanoparticle as the FRET pair.[262] Solid-state glucose fiber optic sensors have been reported in which a QD serves as a FRET donor for an acceptor fluorophore, rendering a ratiometric sensor device.[263–265] In order to exploit direct glucose binding for sensing, QDs have been modified with boronic acid, which form cyclic ethers with saccharides, particularly those with *cis* diols;[266] in some cases, QDs have been immobilized in boronic acid microgels.[267,268] To date, only boronic acid derivatives of viologens have been paired with a QD.[269–271] As a result, we sought to explore alternative fluorophores that exhibit higher glucose selectivity and have an enhanced optical response.

2-Anthrylboronic acid exhibits modest fluorescence quenching upon sugar binding.[272] An analogous system was designed in which an aryl boronic acid is attached to the anthracene fluorophore via a tertiary amine linker (**1** of Figure 9b without the 2-COOH moiety).[273–275] Fluorescence is enhanced in **1** upon glucose binding because photoinduced electron transfer or PET is circumvented.[276,277] In this mechanism (Figure 9a), the lone pair on the amine nitrogen quenches anthracene emission upon photoexcitation by donating an electron into the singly occupied HOMO of the fluorophore. This interaction is disrupted upon binding of the diol at boron, and hence the anthracene fluorescence intensity is enhanced.

Compound **1** was prepared according to literature methods.[278] Previously, this compound has been immobilized in a polymer matrix to afford a solid-state sensor. The carboxylate is needed as functional handle to attach the fluorophore to an amine-functionalized QD. The photophysical properties and glucose sensitivity of **1** were examined for samples prepared in a 1:2 mixture of MeOH and PBS at pH 7.0 at a concentration of ~10 μM. Compound **1** exhibits an absorption maximum at 384 nm and an emission maximum at 437 nm (Figure S2). The absorption profile is unaffected by glucose concentrations of up to 28 mM (Figure S3); thus the FRET efficiency in a QD-**1** construct will be constant. A dramatic emission enhancement is observed upon titrating **1** with a PBS solution of glucose (Figure 10a). At glucose concentrations above ~3 mM, saturation is observed, as seen in the plot of relative emission intensity (I/I_0) at 437 nm versus glucose concentration (Figure 10b). This data was fit to the Hill equation:

$$y = y_{max} \frac{[\text{Glu}]^n}{K_d^n + [\text{Glu}]^n} \quad (6)$$

where K_D is the dissociation constant ($K_D = 1/K_A$) and n is the Hill coefficient, which is a measure of the degree of binding cooperativity. If $n > 1$, then there is positive cooperativity, i.e. the binding of one molecule facilitates subsequent binding events. If $n < 1$, there is negative cooperativity such that the binding of one molecule impedes the binding of additional molecules. If $n = 1$, binding is not cooperative and each binding event is independent. Based on this analysis of the data in Figure 10b, $K_D = 0.43$ mM (or $K_A = 2.3 \times 10^3$ M) and $n = 0.98$. Given this Hill coefficient, glucose binding is not cooperative and each binding event is independent. The equilibrium constant compares favorably to that reported for the derivative of **1** without the 2-COOH moiety (log $K_A = 3.6$),[274] indicating that the presence of a carboxylic acid on the anthracene does not affect the glucose association. While the sensor saturates above 5 mM, a linear response is observed at glucose concentrations below 1 mM (Figure 10c).

To obtain appreciable FRET efficiency in a QD construct, the QD emission should be in the 360–400 nm range to maximize overlap with the absorption of **1** while minimizing overlap with the emission of **1**. To this end, we selected ZnSe as the semiconductor because of its higher bandgap relative to CdSe, thereby enabling access to the desired spectral window.

ZnSe cores were prepared from diethylzinc (ZnEt$_2$) and tri-n-octylphosphine selenide (TOPSe) (see Experimental Methods for details). The growth process was monitored using absorption and emission spectroscopy (Figures S4 and S5, respectively). The absorption and emission spectra of the purified ZnSe QDs are presented in Figure S6. As expected, QD emission nicely overlaps with the absorption profile of **1** (Figure S7) with minimal emission overlap of the two sensor components. Because the QDs exhibited a low quantum yield, they were overcoated with ZnS, using ZnEt$_2$ and bis(trimethylsilyl)sulfide, to passivate the surface. After the addition of the reagents, the QDs were allowed to ripen and this process was monitored by emission spectroscopy (Figure S8). A size-selective precipitation was performed to purify the ZnSe/ZnS core/shell QDs. The two different fractions were monitored with both absorption and emission spectroscopy (Figures S9 and S10, respectively). The larger dots, with a thicker ZnS shell were used, as they exhibited a more intense band edge emission at 380 nm with less intense surface trap emission (broad feature centered at ~475 nm). These ZnSe/ZnS QDs possessed a relative quantum yield of 16%.

Conjugation of **1** to the PIL-coated QDs (25% free amine for dye coupling, Figure 5b) was accomplished using NHS/DCC coupling, but with low yields. Presumably, the terminal amines of the PIL coordinate to the QD surface to reduce the number of conjugation sites on the polymer, resulting in low coupling yields. Alternative coupling methodologies are being explored to increase the conjugation yields[279] including the use of tetrazene and norbornene as a bio-orthogonal reaction pair.[280,281] It has been demonstrated that this coupling strategy is amenable to the PIL ligand.[282] The amine on the free PIL polymer is masked with a carboxylic acid-functionalized norbornene molecule while the carboxylic acid group of the dye is treated with an amine-functionalized tetrazine molecule. QD ligand exchange is performed with the norbornene-modified PIL polymer and finally dye conjugation is accomplished via a Diels-Alder reaction of the norbornene and tetrazene moieties. Studies are currently underway to deliver the construct.

Future Prospects

The development of both solution-based and solid-state sensors remains an active area of research. The former is useful for *in vitro* and *in vivo* biological applications, whereas the latter can be applied to the analysis of *ex vivo* biological samples (i.e., blood or urine), environmental samples, and a variety of other applications. This manuscript has endeavored to introduce relevant principles for developing QD-based sensors for the purposes of providing a metabolic profile of the tumor microenvironment with the goal of providing new tools for the oncologist. One primary concern with the use of QD-based sensors is their toxicity. Overcoating QDs with an inert shell (ZnS or silica) and/or using appropriate surface ligands (amphiphilic polymers) dramatically diminishes QD toxicity, although the long-term leaching of Cd^{2+} ions from the core remains underexplored. Other issues of toxicity involve colloidal instability of the QDs that leads to intracellular aggregation, as well as the generation of reactive oxygen species. These aspects of toxicity have been more fully discussed in several reviews.[118,283,284] For these reasons, the QD-based chemosensors described herein are limited to mouse models. These chemosensors may be extended to study human tumor xenografts in animal models for the measurement of pH, O2, and glucose as a function of therapy or disease progression. Clinicians can then utilize this information to develop chemotherapy dosing regimens that will have a maximal impact on a tumor.

To date, metabolic profiling has been underappreciated by researchers interested in chemosensor design. This is unfortunate as increased activity is needed to presage advances for the development of new therapetutic protocols. Other interesting targets for tumor biology are chemotherapeutics for the clinician to ascertain the quantity of a drug that is

actually delivered to a tumor and biological metabolites of pathways that are affected upon administration of a drug. The fundamental principles and representative examples outlined herein may also be generalized for the development of novel nanosensors for a variety of biologically-relevant analytes (Ca2+, nitric oxide, etc.) for medical applications. Moreover, the approach described herein may be extended beyond the biological milieu. The scope of analyte detection may range from explosives and chemical weapons for security applications, to pollutants and heavy metals for environmental applications.

Concluding Remarks

QDs offer a versatile platform from which to construct nano-scale chemosensors. Because of their tunability and exceptional photophysical properties, they serve as efficient one- and two-photon FRET donors. Developments have been made in QD ligand design to render stable constructs for biological applications. We have demonstrated proof-of-principle for pH and oxygen sensing. QD conjugates of SNARF-5F and porphyrins are sensitive to pH and oxygen, respectively, at biologically relevant analyte concentrations. These constructs have been used for preliminary *in vivo* imaging and sensing. Our studies highlight the challenge of making ratiometric measurements *in vivo* as the different emission wavelengths of the QD and the fluorophore scatter differently, thereby skewing measured ratios as a function of depth. Also, the optical properties of tissue above the imaging plane affect the collection of emitted photons at the objective. We are currently performing simulations to model photon scattering so that quantitative, meaningful ratios can be obtained from *in vivo* intensity data. Though more difficult to collect, lifetime data obviates many of these challenges, and thus this method of detection should prove fruitful. The continued development of QD-fluorophore chemosensors is a worthwhile endeavor that expands the toolkit of oncologists and clinicians to understand fundamental tumor biology and accordingly develop new drug therapeutics and protocols.

Experimental Methods

Preparation of ZnSe/ZnS QDs

The ZnSe cores were prepared by rapidly injecting diethylzinc ($ZnEt_2$) (0.80 mmol) and tri-*n*-octylphosphine selenide (1.0 mmol) dispersed in 4.3 mL tri-*n*-octylphosphine oxide (TOPO) into a round bottom flask containing 7.0 g of degassed hexadecylamine at 310 °C. The flask was then cooled to 270 °C and QD growth was allowed to proceed for 1 h. The crude cores of the reaction mixture were dispersed in hexane and subsequently precipitated using methanol and *n*-butanol and then re-dissolved in hexane ($\lambda_{PL,max}$ = 363 nm). The ZnSe cores were further modified with a ZnS shell. The cores were dissolved in TOPO (8 g) and *n*-hexylphosphonic acid (1.9 mmol) and heated to 160 °C under vacuum. Then a $ZnEt_2$ solution (0.41 mmol in 2.75 mL tri-*n*-octylphosphine (TOP)) and a bis(trimethylsilyl)sulfide solution (0.41 mmol in 2.75 mL TOP) were slowly added (0.5 mL/minute). The QDs were then annealed at 80 °C overnight. The reaction mixture was dissolved in hexanes and then precipitated with methanol and *n*-butanol (1st precipitation of Figures S9 and S10, $\lambda_{PL,max}$ = 380 nm). The recovered supernatant was precipitated with methanol (2nd precipitation of Figures S9 and S10, $\lambda_{PL,max}$ = 375 nm). All precipitated QDs were resuspended in hexane.

Physical Measurements

UV–vis absorption spectra were acquired using a Cary 5000 spectrometer. Steady-state emission spectra were recorded on an automated Photon Technology International (PTI) QM 4 fluorometer equipped with a 150 W Xe arc lamp and a Hammamatsu R2658 photomultiplier tube. The relative quantum yield of QDs (Φ_{sam}) was calculated using anthracene in cyclohexane as the reference according to the following equation,

$$\Phi_{\mathrm{sam}} = \Phi_{\mathrm{ref}} \left(\frac{A_{\mathrm{ref}}}{A_{\mathrm{sam}}} \right) \left(\frac{I_{\mathrm{sam}}}{I_{\mathrm{ref}}} \right) \left(\frac{\eta_{\mathrm{sam}}}{\eta_{\mathrm{ref}}} \right)^2 \quad (7)$$

where A is the measured absorbance, η is the refractive index of the solvent, I is the integrated emission intensity, and Φ_{ref} is the emission quantum yield of the reference. Φ_{ref} was taken to be 0.36 for a sample of anthracene in cyclohexane.[285]

Multiphoton Imaging

Two-photon lifetime measurements were made using a custom-built multiphoton laser-scanning microscope (MPLSM) in the Edwin L. Steele Laboratory, Department of Radiation Oncology at Massachusetts General Hospital, as previously described.[96] Sub-100 fs laser pulses were generated at a repetition rate of 80 MHz in a mode-locked Ti:sapphire oscillator (Spectra-Physics Mai Tai HP), which was pumped by a 14 W cw Spectra-Physics Millennia diode-pumped solid-state (DPSS) laser operating at 532 nm; the output of the Mai Tai laser was tunable over the 690–1040 nm range. The laser output was adjusted using a 10RP52-2 zero-order half-wave plate (Newport) and a 10GL08AR.16 Glan-Laser polarizer (Newport) to attenuate the power. The laser beam was directed into a custom-modified multiphoton microscope based on the Olympus Fluoview 300 laser scanner. The output beam from the scanner was collimated through a scan lens into the back of an Olympus BX61WI microscope. An Olympus LUMPlanFL 20×, 0.95 NA water immersion objective lens was used to focus the excitation light and collect the emission light. NIR laser excitation light and visible emission light were separated using a 750SP-2P AR-coated dichroic mirror (Chroma Technology).

This MPLSM system was used to collect two-photon *in vivo* images of severe combined immunodeficient (SCID) mice with surgically implanted cranial windows, as previously described.[286] Prior to imaging, mice were with anesthetized with Ketamine/Xylazine (10/1 mg/mL) and subsequently treated with 150–200 μL of the QD-porphyrin micelle oxygen sensor solution via retro-orbital injection. For imaging, 850 nm excitation light was used at a power of 400 mW. Collected light was split into three optical channels: green for QD emission using a 570 nm dichroic mirror and a 535/40 bandpass filter, yellow for autofluorescence using a 585 nm dichroic mirror, and red for porphyrin emission using a 690/90 bandpass filter. Each channel was directed into a GaAs H7421-50 photomultipler tube (Hamamatsu). After imaging, mice were sacrificed with a systemic injection of Fatal-Plus.

For tumor imaging, SCID mice with surgically implanted dorsal skinfold chambers (DSC)[287] were implanted with a piece of LS174T human colorectal adenocarcinoma tumor (~1 mm diameter) from a serially passaged subcutaneous *in vivo* source from the same murine background in the center of the chamber. After 1–2 weeks, the tumor was of appropriate size to conduct experiments (~4 mm in diameter). Prior to imaging, mice were anesthetized with isoflurane. The coverslip of the DSC was removed and a solution of the QD-SNARF-5F sensor was applied to the tumor and allowed to diffuse for 5 minutes prior to replacing the coverslip. Cascade blue dextran (~500 kDa MW) was administered by intraperiotneal (i.p.) injection to image the vasculature. To monitor pH changes in response to glucose administration, glucose (6 g/kg) was injected i.p. and the tumor was imaged every 10 min for 90 min. For imaging, 800 nm excitation light was used at a power of 40 mW. Collected light was split into three optical channels: blue for Cascade blue dextran, green for QD emission using a 565 nm shortpass dichroic mirror and a 535/40 bandpass filter, and red for SNARF-5F emission using a 660/50 bandpass filter. Each channel was directed into an HC125-02 photomultiplier tube (Hamamatsu). After imaging, mice were sacrificed with a systemic injection of Fatal-Plus.

Supplementary Material

Refer to Web version on PubMed Central for supplementary material.

Acknowledgments

References

1. Arnold MA, Small GW. Anal Chem. 2005; 77:5429–5439. [PubMed: 16131049]

2. Aslan K, Zhang J, Lackowicz JR, Geddes CD. J Fluoresc. 2004; 14:391–400. [PubMed: 15617381]

3. Ballerstadt R, Evans C, McNichols R, Gowda A. Biosens Bioelectron. 2006; 22:275–284. [PubMed: 16488598]

4. Kondepati VR, Heise HM. Anal Bioanal Chem. 2007; 388:545–563. [PubMed: 17431594]

5. Pickup JC, Hussain F, Evans ND, Rolinski OJ, Birch DJS. Biosens Bioelectron. 2005; 20:2555–2565. [PubMed: 15854825]

6. Wang J. Chem Rev. 2008; 108:814–825. [PubMed: 18154363]

7. Cable ML, Kirby JP, Sorasaenee K, Gray HB, Ponce A. J Am Chem Soc. 2007; 129:1474–1475. [PubMed: 17243674]

8. Yung PT, Lester ED, Bearman G, Ponce A. Biotechnol Bioeng. 2007; 98:864–871. [PubMed: 17514759]

9. Royo S, Martinez-Manez R, Sancenon F, Costero AM, Parra M, Gil S. Chem Commun. 2007:4839–4847.

10. Jiang Y, Zhao H, Zhu N, Lin Y, Yu P, Mao L. Angew Chem Int Ed. 2008; 47:8601–8604.

11. Gao D, Wang Z, Liu B, Ni L, Wu M, Zhang Z. Anal Chem. 2008; 80:8545–8553. [PubMed: 18847285]

12. Ai K, Zhang B, Lu L. Angew Chem Int Ed. 2009; 48:304–308.

13. Oh WK, Jeong YS, Song J, Jang J. Biosens Bioelectron. 2011; 29:172–177. [PubMed: 21893406]

14. Koochesfahani, MM.; Nocera, DG. Handbook of Experimental Fluid Mechanics. Tropea, C.; Foss, JF.; Yarin, A., editors. Springer–Verlag; Heidelberg: 2007. p. 362-382.

15. Pouya S, Koochesfahani MM, Snee P, Bawendi MG, Nocera DG. Exp Fluids. 2005; 39:784–786.

16. Pouya S, Koochesfahani MM, Greytak AB, Bawendi MG, Nocera DG. Exp Fluids. 2008; 44:1035–1038.

17. Hu H, Jin Z, Nocera D, Lum C, Koochesfahani M. Meas Sci Technol. 2010; 21:085401-1–085401-14.

18. Ji HF, Shen Y, Hubner JP, Carroll BF, Schmehl RH, Simon JA, Schanze KS. Appl Spectrosc. 2000; 54:856–863.

19. Carroll BF, Hubner JP, Schanze KS, Bedlek-Anslow JM. J Visual. 2001; 4:121–129.

20. Dale GA, Gross LP, Watkins AN, Nocera DG. Proc Int Instrum Symp. 2001; 47:10–25.

21. Carroll BF, Abbitt JD, Lukas EW, Morris MJ. AIAA J. 1996; 34:521–526.

22. Schanze KS, Carroll BF, Korotkevitch S, Morris MJ. AIAA J. 1997; 35:306–310.

23. Niessner R. Trends Anal Chem. 1991; 10:310–316.

24. Scully P, Chandy R, Edwards R, Merchant D, Morgan R. Environ Sci Res. 2001; 56:175–199.

25. Szmacinski H, Lakowicz JR. Sens Actuators, B. 1995; B29:16–24.

26. Wang L, Wang L, Xia T, Dong L, Bian G, Chen H. Anal Sci. 2004; 20:1013–1017. [PubMed: 15293393]

27. Ma C, Zeng F, Huang L, Wu S. J Phys Chem B. 2011; 115:874–882. [PubMed: 21250732]

28. Su S, Wu W, Gao J, Lu J, Fan C. J Mater Chem. 2012; 22:18101–18110.

29. Kim HN, Ren WX, Kim JS, Yoon J. Chem Soc Rev. 2012; 41:3210–3244. [PubMed: 22184584]

30. Dosev, D.; Nichkova, M.; Kennedy, IM. Environmental Applications of Nanomaterials. 2. Fryxel, GE.; Cao, G., editors. Imperial College Press; London: 2012. p. 561-619.

31. Du, D. Environmental Applications of Nanomaterials. 2. Fryxel, GE.; Cao, G., editors. Imperial College Press; London: 2012. p. 621-645.

32. Bell T, Hext NM. Chem Soc Rev. 2004; 33:589–598. [PubMed: 15592624]

33. de Silva AP, Gunaratne HQN, Gunnlaugsson T, Huxley AJM, McCoy CP, Rademacher JT, Rice TE. Chem Rev. 1997; 97:1515–1566. [PubMed: 11851458]

34. Desvergne, JP.; Czarnik, AW., editors. Chemosensors of Ion and Molecular Recognition. Kluwer Academic; Dordrecht, The Netherlands: 1997. p. 492

35. Czarnik, AW., editor. Fluorescent Chemosensors for Ion and Molecule Recognition. American Chemical Society; Washington, D.C: 1993.

36. Czarnik AW. Acc Chem Res. 1994; 27:302–308.

37. Rudzinski CM, Hartmann WK, Nocera DG. Coord Chem Rev. 1998; 171:115–123.

38. Rudzinski, CM.; Nocera, DG. Optical Sensors and Switches. Ramamurthy, V.; Schanze, KS., editors. Marcel Dekker; New York: 2001. p. 1-91.

39. Rudzinski CM, Young AM, Nocera DG. J Am Chem Soc. 2002; 124:1723–1727. [PubMed: 11853449]

40. Swager TM. Acc Chem Res. 1998; 31:201–207.

41. Mohr GJ. Chem Eur J. 2004; 10:1082–1090. [PubMed: 15007799]

42. de Silva AP, Fox DB, Moody TS, Weir SM. Trends Biotechnol. 2001; 19:29–34. [PubMed: 11146100]

43. Rudzinski CM, Young AM, Nocera DG. J Am Chem Soc. 2002; 124:1723–1727. [PubMed: 11853449]

44. Wun AW, Snee PT, Chan Y, Bawendi MG, Nocera DG. J Mater Chem. 2005; 15:2697–2706.

45. Wolfbeis OS. J Mater Chem. 2005; 15:2657–2669.

46. Lakowicz, JR. Principles of Fluorescence Spectroscopy. 3. Springer; New York: 2006.

47. Campbell CG, Ghodrati M, Garrido F. Soil Sci. 1999; 164:156–170.

48. O'Connell KP, Valdes JJ, Azer NL, Schwartz RP, Wright J, Eldefrawi ME. J Immunol Meth. 1999; 225:157–169.

49. Verhey HJ, Gebben B, Hofstraat JW, Verhoeven JW. J Polym Sci Part A: Polym Chem. 1995; 33:399–405.

50. Tan W, Shi ZY, Smith S, Birnbaum D, Kopelman R. Science. 1992; 258:778–781. [PubMed: 1439785]

51. Sharp SL, Warmack RJ, Goudinnet JP, Lee I, Ferrell TL. Acc Chem Res. 1993; 26:377–382.

52. Dahan M, Levi S, Luccardini C, Rostaing P, Riveau B, Triller A. Science. 2003; 302:442–445. [PubMed: 14564008]

53. Shimizu KT, Neuhauser RG, Leatherdale CA, Empedocies SA, Woo WK, Bawendi MG. Phys Rev B. 2001; 63:205316/1–5.

54. Xie XS, Lu HP. Springer Ser Chem Phys. 2001; 67:227–240.

55. Deniz AA, Dahan M, Grunwell JR, Ha T, Faulhaver AE, Chemla DS, Weiss S, Schultz PG. Proc Natl Acad Sci USA. 1999; 96:3670–3675. [PubMed: 10097095]

56. Weiss S. Science. 1999; 283:1676–1683. [PubMed: 10073925]

57. Ha T, Ting AY, Liang J, Caldwell WB, Deniz AA, Chemla DS, Schultz PG, Weiss S. Proc Natl Acad Sci USA. 1999; 96:893–898. [PubMed: 9927664]

58. Chan Y, Snee PT, Caruge JM, Yen BK, Nair GP, Nocera DG, Bawendi MG. J Am Chem Soc. 2006; 128:3146–3147. [PubMed: 16522086]

59. Sundar VC, Eisler HJ, Deng T, Chan Y, Thomas EL, Bawendi MG. Adv Mater. 2004; 16:2137–2141.

60. Vezenov DV, Mayers BT, Conroy RS, Whitesides GM, Snee PT, Chan Y, Nocera DG, Bawendi MG. J Am Chem Soc. 2005; 127:8952–8953. [PubMed: 15969563]

61. Murray CB, Norris DJ, Bawendi MG. J Am Chem Soc. 1993; 115:8706–8715.

62. Bawendi MC, Steigerwald ML, Brus LE. Annu Rev Phys Chem. 1990; 41:477–496.

63. Kastner MA. Phys Today. 1993; 46:24–31.

64. Anscombe N. N Photonics. 2007; 1:360–361.

65. Azzazy HME, Mansour MMH, Kazmierczak SC. Clin Biochem. 2007; 40:917–927. [PubMed: 17689518]

66. Hammer NI, Emrick T, Barnes MD. Nanosci Res Lett. 2007; 2:282–290.

67. Coe-Sullivan S. Mater Matters. 2007; 2:13–14.

68. Corbin JG, Haydar TF. Nanomed. 2007; 2:579–581.

69. Guyot-Sionnest P. Mater Matters. 2007; 2:10–12.

70. Pinaud F, Michalet X, Bentolila LA, Tsay JM, Doose S, Li JJ, Iyer G, Weiss S. Biomater. 2006; 27:1679–1687.

71. Reithmaier JP, Somers A, Kaiser W, Deubert S, Gerschuetz F, Forchel A, Parillaud O, Krakowski M, Alizon R, Hadass D, Bilenca A, Dery H, Mikhelashvili V, Eisenstein G, Gioannini M, Montrosset I, Berg TW, van der Poel M, Mork J, Tromborg B. Phys Status Solidi B. 2006; 243:3981–3987.

72. Samia ACS, Dayal S, Burda C. Photochem Photobiol. 2006; 82:617–625. [PubMed: 16475871]

73. Scholz M, Aichele T, Benson O. Adv Sol State Phys. 2008; 46:3–14.

74. Wu MH, Ueda A, Mu R. Opt Sci Eng. 2005; 99:331–350.

75. Walker GW, Sundar VC, Rudzinski CM, Wun AW, Bawendi MG, Nocera DG. Appl Phys Lett. 2003; 83:3555–3557.

76. Kittel, C. Introduction to Solid State Physics. 8. John Wiley & Sons; Hoboken, NJ: 2005.

77. Brus LE. J Chem Phys. 1983; 79:5566–5571.

78. de Mello Donegá C. Chem Soc Rev. 2011; 40:1512–1546. [PubMed: 20972490]

79. Alvisatos AP. J Phys Chem. 1996; 100:13226–13239.

80. Hines MA, Guyot-Sionnest P. J Phys Chem. 1996; 100:468–471.

81. Dabbousi BO, Rodriguez-Viejo J, Mikulec FV, Heine JR, Mattoussi H, Ober R, Jensen KF, Bawendi MG. J Phys Chem B. 1997; 101:9463–9475.

82. Greytak AB, Allen PM, Liu W, Zhao J, Young ER, Popovic Z, Walker BJ, Nocera DG, Bawendi MG. Chem Sci. 2012; 3:2028–2034.

83. Jaiswal JK, Simon SM. Trends Cell Biol. 2004; 14:497–504. [PubMed: 15350978]

84. Medintz IL, Uyeda HT, Goldman ER, Mattoussi H. Nat Mater. 2005; 4:435–446. [PubMed: 15928695]

85. Michalet X, Pinaud FF, Bentolila LA, Tsay JM, Doose S, Li JJ, Sundaresan G, Wu AM, Gambhir SS, Weiss S. Science. 2005; 307:538–544. [PubMed: 15681376]

86. Dubertret B, Skourides P, Norris DJ, Noireaux V, Brivanlou AH, Libchaber A. Science. 2002; 298:1759–1762. [PubMed: 12459582]

87. Jain RK, Stroh M. Nat Biotechnol. 2004; 22:959–960. [PubMed: 15286644]

88. Wu X, Liu H, Liu J, Haley KN, Treadway JA, Larson JP, Ge N, Peale F, Bruchez MP. Nat Biotechnol. 2003; 21:41–46. [PubMed: 12459735]

89. Gao X, Cui Y, Levenson RM, Chung LW, Nie S. Nat Biotechnol. 2004; 22:969–976. [PubMed: 15258594]

90. Stroh M, Zimmer JP, Duda DG, Levchenko TS, Cohen KS, Brown EB, Scadden DT, Torchilin VP, Bawendi MG, Fukumura D, Jain RK. Nat Med. 2005; 11:678–682. [PubMed: 15880117]

91. Somers RC, Bawendi MG, Nocera DG. Chem Soc Rev. 2007; 36:579–591. [PubMed: 17387407]

92. Förster T. Ann Phys. 1948; 437:55–75.

93. König K. J Microsc. 2000; 200:83–104. [PubMed: 11106949]

94. Pawlicki M, Collins HA, Denning RG, Anderson HL. Angew Chem Int Ed. 2009; 48:3244–3266.

95. Squirrell JM, Wokosin DL, White JG, Bavister BD. Nat Biotechnol. 1999; 17:763–767. [PubMed: 10429240]

96. Brown EB, Campbell RB, Tsuzuki Y, Xu L, Carmeliet P, Fukumura D, Jain RK. Nat Med. 2001; 7:864–868. [PubMed: 11433354]

97. Jain RK, Munn LL, Fukumura D. Nat Rev Cancer. 2002; 2:266–276. [PubMed: 12001988]

98. Xu C, Zipfel W, Shear JB, Williams RM, Webb WW. Proc Natl Acad Sci USA. 1996; 93:10763–10768. [PubMed: 8855254]

99. Jain, RK.; Booth, MF.; Padera, TP.; Munn, LL.; Fukumura, D.; Brown, E. Applications of Nonlinear Intravital Microscopy in Tumor Biology. In: Masters, BR.; So, PTC., editors. Handbook of Biomedical Nonlinear Optical Microscopy. Oxford University Press; New York: 2008. p. 735-756.

100. Zipfel WR, Williams RM, Webb WW. Nat Biotechnol. 2003; 21:1369–1377. [PubMed: 14595365]

101. Helmchen F, Denk W. Nat Meth. 2005; 2:932–940.

102. Birge, RR. One-Photon and Two-Photon Excitation Spectroscopy. In: Klinger, DS., editor. Ultrasensitive Laser Spectroscopy. Academic Press; New York: 1983. p. 109-174.

103. Xu, C.; Zipfel, WR. Multiphoton Excitation of Fluorescent Probes. In: Masters, BR.; So, PTC., editors. Handbook of Biomedical Nonlinear Optical Microscopy. Oxford University Press; New York: 2008. p. 311-333.

104. Xu C, Webb WW. J Opt Soc Am B. 1996; 13:481–491.

105. Albota MA, Xu C, Webb WW. Appl Opt. 1998; 37:7352–7356. [PubMed: 18301569]

106. Oulianov DA, Tomov IV, Dvornikov AS, Rentzepis PM. Opt Commun. 2001; 191:235–243.

107. Albota M, Beljonne D, Brédas JL, Ehrlich JE, Fu JY, Heikal AA, Hess SE, Kogej T, Levin MD, Marder SR, McCord-Maughon D, Perry JW, Röckel H, Rumi M, Subramaniam G, Webb WW, Wu XL, Xu C. Science. 1998; 281:1653–1656. [PubMed: 9733507]

108. Blanton SA, Dehestani A, Lin PC, Guyot-Sionnest P. Chem Phys Lett. 1994; 229:317–322.

109. Larson DR, Zipfel WR, Williams RM, Clark SW, Bruchez MP, Wise FW, Webb WW. Science. 2003; 300:1434–1436. [PubMed: 12775841]

110. Pu SC, Yang MJ, Hsu CC, Lai CW, Hsieh CC, Lin SH, Cheng YM, Chou PT. Small. 2006; 2:1308–1313. [PubMed: 17192978]

111. Schmidt ME, Blanton SA, Hines MA, Guyot-Sionnest P. Phys Rev B. 1996; 53:12629–12632.

112. Blanton SA, Hines MA, Schmidt ME, Guyot-Sionnest P. J Lumin. 1996; 70:253–268.

113. Jain RK. Science. 2005; 307:58–62. [PubMed: 15637262]

114. Vaupel P, Kallinowski F, Okunieff P. Cancer Res. 1989; 49:6449–6465. [PubMed: 2684393]

115. Helmlinger G, Yuan F, Dellian M, Jain RK. Nat Med. 1997; 3:177–182. [PubMed: 9018236]

116. Sapsford KE, Pons T, Medintz IL, Mattoussi H. Sensors. 2006; 6:925–953.

117. Medintz IL, Mattoussi H. Phys Chem Chem Phys. 2009; 11:17–45. [PubMed: 19081907]

118. Mattoussi H, Palui G, Na HB. Adv Drug Delivery Rev. 2012; 64:138–166.

119. Warburg O, Posener K, Negelein E. Biochem Z. 1924; 152:319–344.

120. Warburg O. Science. 1956; 123:309–314. [PubMed: 13298683]

121. Cairns RA, Harris IS, Mak TW. Nat Rev Cancer. 2011; 11:85–95. [PubMed: 21258394]

122. Helmlinger G, Sckell A, Dellian M, Forbes NS, Jain RK. Clin Cancer Res. 2002; 8:1284–1291. [PubMed: 11948144]

123. Fukumura D, Jain RK. Microvasc Res. 2007; 74:72–84. [PubMed: 17560615]

124. Fukumura D, Jain RK. J Cell Biochem. 2007; 101:937–949. [PubMed: 17171643]

125. Erler JT, Bennewith KL, Nicolau M, Dornhoefer N, Kong C, Le QT, Chi JT, Jeffrey SS, Giaccia AJ. Nature. 2006; 440:1222–1226. [PubMed: 16642001]

126. Pennacchietti S, Michieli P, Galluzzo M, Mazzone M, Giordano S, Comoglio PM. Cancer Cell. 2003; 3:347–361. [PubMed: 12726861]

127. Rofstad EK, Mathiesen B, Kindem K, Galappathi K. Cancer Res. 2006; 66:6699–6707. [PubMed: 16818644]

128. Folkman J. N Engl J Med. 1971; 285:1182–1186. [PubMed: 4938153]

129. Carmeliet R, Jain RK. Nature. 2000; 407:249–257. [PubMed: 11001068]

130. Jain RK. Nat Med. 2001; 7:987–989. [PubMed: 11533692]

131. Folkman J. Nat Rev Drug Discovery. 2007; 6:273–286.

132. Chauhan VP, Stylianopoulos T, Boucher Y, Jain RK. Annu Rev Chem Biomol Eng. 2011; 2:281–298. [PubMed: 22432620]

133. Carmeliet P, Jain RK. Nat Rev Drug Discovery. 2011; 10:417–427.

134. Carmeliet P. Nature. 2005; 438:932–936. [PubMed: 16355210]

135. Yuan F, Chen Y, Dellian M, Safabakhsh N, Ferrara N, Jain RK. Proc Natl Acad Sci USA. 1996; 93:14765–14770. [PubMed: 8962129]

136. Lee CG, Heijn M, di Tomaso E, Griffon-Etienne G, Ancukiewicz M, Koike C, Park KR, Ferrara N, Jain RK, Suit HD, Boucher Y. Cancer Res. 2000; 60:5565–5570. [PubMed: 11034104]

137. Yang JC, Haworth L, Sherry RM, Hwu P, Schwartzentruber DJ, Topalian SL, Steinberg SM, Chen HX, Rosenberg SA. N Engl J Med. 2003; 349:427–434. [PubMed: 12890841]

138. Cobleigh M, Langmuir VK, Sledge GW, Miller KD, Haney L, Novotny WF, Reimann JD, Vassel A. Semin Oncol. 2003; 30:117–124. [PubMed: 14613032]

139. Mayer R. N Engl J Med. 2004; 350:2406–2408. [PubMed: 15175443]

140. Conley SJ, Gheordunescu E, Kakarala P, Newman B, Korkaya H, Heath AN, Clouthier SG, Wicha MS. Proc Natl Acad Sci USA. 2012; 109:2784–2789. [PubMed: 22308314]

141. Dean M, Fojo T, Bates S. Nat Rev Cancer. 2005; 5:275–284. [PubMed: 15803154]

142. Li L, Neaves WB. Cancer Res. 2006; 66:4553–6458. [PubMed: 16651403]

143. Keith B, Simon MC. Cell. 2007; 129:465–472. [PubMed: 17482542]

144. Mohyeldin A, Garzón-Muvdi T, Quiñones-Hinojosa A. Cell Stem Cell. 2010; 7:150–161. [PubMed: 20682444]

145. Rasheed ZA, Kowalski J, Smith BD, Matsui W. Stem Cells. 2011; 29:883–887. [PubMed: 21509907]

146. Ping YF, Bian XW. Stem Cells. 2011; 29:888–894. [PubMed: 21557392]

147. Takaura N. Cancer Sci. 2012; 103:1177–1181. [PubMed: 22416970]

148. Mathieu J, Zhang Z, Zhou W, Wang AJ, Heddleston JM, Pinna CMA, Hubaud A, Stadler B, Choi M, Bar M, Tewari M, Liu A, Vessella R, Rostomily R, Born D, Horwitz M, Ware C, Blau CA, Cleary MA, Rich JN, Ruohola-Baker H. Cancer Res. 2011; 71:4640–4652. [PubMed: 21712410]

149. Qiang L, Wu T, Zhang HW, Lu N, Hu R, Wang YJ, Zhao L, Chen FH, Wang XT, You QD, Guo QL. Cell Death Differ. 2012; 19:284–294. [PubMed: 21818118]

150. Pàez-Ribes M, Allen E, Hudock J, Takeda T, Okuyama H, Viñals F, Inoue M, Bergers G, Hanahan D, Casanovas O. Cancer Cell. 2009; 15:220–231. [PubMed: 19249680]

151. Conley SJ, Wicha MS. Proc Natl Acad Sci USA. 2012; 109:E915.

152. Hurwitz H, Fehrenbacher L, Novotny W, Cartwright T, Hainsworth J, Heim W, Berlin J, Baron A, Griffing S, Holmgren E, Ferrara N, Fyfe G, Rogers B, Ross R, Kabbinavar F. N Engl J Med. 2004; 350:2335–2342. [PubMed: 15175435]

153. Ma J, Pulfer S, Li S, Chu J, Reed K, Gallo JM. Cancer Res. 2001; 61:5491–5498. [PubMed: 11454697]

154. Murata R, Nishumura Y, Hiraoka M. Int J Radiat Oncol. 1997; 37:1107–1113.

155. Fenton BM, Paoni SF, Ding I. Radiother Oncol. 2004; 72:221–230. [PubMed: 15297140]

156. Hansen-Algenstaedt N, Stoll BR, Padera TP, Dolmans DEJGJ, Hicklin DJ, Fukumura D, Jain RK. Cancer Res. 2000; 60:4556–4560. [PubMed: 10969807]

157. Brown JM. Cancer Res. 1999; 59:5863–5870. [PubMed: 10606224]

158. Bruchez M, Moronne M, Gin P, Weiss S, Alivisatos AP. Science. 1998; 281:2013–2016. [PubMed: 9748157]

159. Chan WC, Nie S. Science. 1998; 281:2016–2018. [PubMed: 9748158]

160. Chen Y, Thakar R, Snee PT. J Am Chem Soc. 2008; 130:3744–3745. [PubMed: 18321112]

161. Guo W, Li JJ, Wang YA, Peng X. Chem Mater. 2003; 15:3125–2133.

162. Guo W, Li JJ, Wany YA, Peng X. J Am Chem Soc. 2003; 125:3901–3909. [PubMed: 12656625]

163. Huang B, Tomalia DA. Inorg Chem Acta. 2006; 359:1961–1966.

164. Liu Y, Kim M, Wang Y, Wang YA, Peng X. Langmuir. 2006; 22:6341–6345. [PubMed: 16800696]

165. Wang YA, Li JJ, Chen H, Peng X. J Am Chem Soc. 2002; 124:2293–2298. [PubMed: 11878983]

166. Wisher AC, Bronstein I, Chechik V. Chem Commun. 2006:1637–1639.

167. Kim S, Bawendi MG. J Am Chem Soc. 2003; 125:14652–14653. [PubMed: 14640609]

168. Uyeda HT, Medintz IL, Jaiswal JK, Simon SM, Mattoussi H. J Am Chem Soc. 2005; 127:3870–3878. [PubMed: 15771523]

169. Shtykova EV, Huang X, Gao X, Dyke JC, Schumucker AL, Dragnea B, Remmes N, Baxter DV, Stein B, Konarev PV, Svergun DI, Bronstein LM. J Phys Chem C. 2008; 112:16809–16817.

170. Zylstra J, Amey J, Miska NJ, Pang L, Hine CR, Langer L, Dyole RP, Maye MM. Langmuir. 2011; 27:4371–4379. [PubMed: 21410215]

171. Hezinger, AFE.; Goepferich, AM.; Tessmar, JK. Handbook of Nanophysics: Nanoparticles and Quantum Dots. Sattler, KD., editor. Vol. 36. CRC Press; Boca Raton, FL: 2010. p. 1-15.

172. Liu W, Howarth M, Greytak AB, Zheng Y, Nocera DG, Ting AY, Bawendi MG. J Am Chem Soc. 2008; 130:1274–1284. [PubMed: 18177042]

173. Liu W, Greytak AB, Lee J, Wong CR, Park J, Marshall LF, Jiang W, Curtin PN, Ting AY, Nocera DG, Fukumura D, Jain RK, Bawendi MG. J Am Chem Soc. 2010; 132:472–483. [PubMed: 20025223]

174. Susumu K, Uyeda HT, Medintz IL, Pons T, Delehanty JB, Mattoussi H. J Am Chem Soc. 2007; 129:13987–13996. [PubMed: 17956097]

175. Mei BC, Susumu K, Medintz IL, Delehanty JB, Mountziaris TJ, Mettoussi H. J Mater Chem. 2008; 18:4949–4958.

176. Susumu K, Mei BC, Mattoussi H. Nat Protoc. 2009; 3:424–436. [PubMed: 19265801]

177. Moad G, Rizzardo E, Thang SH. Aust J Chem. 2005; 58:379–410.

178. Popovic Z, Liu W, Chauhan VP, Lee J, Wong C, Greytak AB, Insin N, Nocera DG, Fukumura D, Jain R, Bawendi MG. Angew Chem Int Ed. 2010; 49:8649–8652.

179. Gao M, Kirstein S, Möhwald Rogach AL, Kornowski A, Eychmüller A, Weller H. J Phys Chem B. 1998; 102:8360–8363.

180. Zhang H, Zhou Z, Yang B, Gao M. J Phys Chem B. 2003; 107:8–13.

181. Deng Z, Zhang Y, Yue J, Tang F, Wei Q. J Phys Chem B. 2007; 111:12024–12031. [PubMed: 17887667]

182. Yun Z, Zhengtao D, Jiachang Y, Fangqiong T, Qun W. Anal Biochem. 2007; 364:122–127. [PubMed: 17400169]

183. Leitão JMM, Gonçalves H, Mendonça C, da Silva JCGE. Anal Chim Acta. 2008; 628:143–154. [PubMed: 18929002]

184. Wang YQ, Ye C, Zhu ZH, Hu YZ. Anal Chim Acta. 2008; 610:50–56. [PubMed: 18267139]

185. Maule C, Gonçalves H, Mendonça C, Sampaio P, da Silva JCGE, Jorge P. Talanta. 2010; 80:1932–1938. [PubMed: 20152435]

186. Susha AS, Javierr AM, Parak WJ, Rogach AL. Colloids Surf A. 2006; 281:40–43.

187. Zavgorodnya O, Kharlampieva E, Lilly GD, Kotov NA, Tsukruk VV. Polym Prepr. 2009; 50:587.

188. Kharlampieva E, Kozlovskaya V, Zavgorodnya O, Lilly GD, Kotov NA, Tsukruk VV. Soft Matter. 2010; 6:800–807.

189. Ye S, Shen C, Pang H, Wang J, Lu Y. Polymer. 2011; 52:2542–2549.

190. Serrano IC, Ma Q, Palomares E. J Mater Chem. 2011; 21:17673–17679.

191. Generalova AN, Oleinikov VA, Zarifullina MM, Lankina EV, Sizova SV, Artemyev MV, Zubov VP. J Colloid Interface Sci. 2011; 357:265–272. [PubMed: 21377163]

192. Gao X, Chan WCW, Nie S. J Biomed Opt. 2002; 7:532–537. [PubMed: 12421118]

193. Liu YS, Sun Y, Vernier PT, Liang CH, Chong SYC, Gundersen MA. J Phys Chem C. 2007; 111:2872–2878.

194. Zhu S, Zhang J, Liu X, Li B, Wang X, Tang S, Meng Q, Li Y, Shi C, Hu R, Yang B. RSC Adv. 2012; 2:2717–2720.

195. Hardzei M, Artemyev M. J Lumin. 2012; 132:425–428.

196. Paek K, Chung S, Cho CH, Kim BJ. Chem Commun. 2011; 47:10272–10274.

197. Riedinger A, Leal MP, Deka SR, George C, Franchini IR, Falqui A, Cingolani R, Pellegrino T. Nano Lett. 2011; 11:3136–3141. [PubMed: 21692456]

198. Wu W, Shen J, Banerjee P, Zhou S. Biomater. 2010; 31:8371–8381.

199. Wu W, Aiello M, Zhou T, Berliner A, Banerjee P, Zhou S. Biomater. 2010; 31:3023–3031.

200. Wu Y, Chakrabortty S, Gropeanu RA, Wilhelmi J, Xu Y, Er KS, Kuan SL, Koynov K, Chan Y, Weil T. J Am Chem Soc. 2010; 132:5012–5014. [PubMed: 20302298]

201. Maikap S, Prakash A, Banerjee W, Das A, Lai CS. Microelectron Reliab. 2010; 50:747–752.

202. Dennis AM, Bao G. Proc SPIE. 2010; 7575:75750C/1–9.

203. Dennis AM, Rhee WJ, Sotto D, Dublin SN, Bao G. ACS Nano. 2012; 6:2917–2924. [PubMed: 22443420]

204. Tomasulo M, Yildiz I, Raymo FM. J Phys Chem B. 2006; 110:3853–3855. [PubMed: 16509664]

205. Tomasulo M, Yildiz I, Kaanumalle SL, Raymo FM. Langmuir. 2006; 22:10284–10290. [PubMed: 17107034]

206. Medintz IL, Stewart MH, Trammell SA, Susumu K, Delehanty JB, Mei BC, Melinger JS, Blanco-Canosa JB, Dawson PE, Mattoussi H. Nat Mater. 2010; 9:676–684. [PubMed: 20651808]

207. Ji X, Palui G, Avellini T, Na HB, Yi C, Knappenberger KL, Mattoussi H. J Am Chem Soc. 2012; 134:6006–6017. [PubMed: 22394283]

208. Suzuki M, Husimi Y, Komatsu H, Suzuki K, Douglas KT. J Am Chem Soc. 2008; 130:5720–5725. [PubMed: 18393422]

209. Jin T, Sasaki A, Kinjo M, Miyazaki J. Chem Commun. 2010; 46:2408–2410.

210. Gui R, An X, Huang W. Anal Chim Acta. 2013; 767:134–140. [PubMed: 23452797]

211. Tang R, Lee H, Achilefu S. J Am Chem Soc. 2012; 134:4545–4548. [PubMed: 22360301]

212. Coto-Garcia AM, Fernández-Argüelles MT, Costa-Fernández JM, Sanz-Medel A. Chem Commun. 2009:5454–5456.

213. Wang X, Boschetti C, Ruedas-Rama MJ, Tunnacliffe A, Hall EAH. Analyst. 2010; 135:1585–1591. [PubMed: 20449508]

214. Hiruta Y, Yoshizawa N, Citterio D, Suzuki K. Anal Chem. 2012; 84:10650–10656. [PubMed: 23163876]

215. Snee PT, Somers RC, Nair G, Zimmer JP, Bawendi MG, Nocera DG. J Am Chem Soc. 2006; 128:13320–13321. [PubMed: 17031920]

216. Somers RC, Lanning RM, Snee PT, Greytak AB, Jain RK, Bawendi MG, Nocera DG. Chem Sci. 2012; 3:2980–2985.

217. Bashkatov AN, Genina EA, Kochubey VI, Tuchin VV. J Phys D: Appl Phys. 2005; 38:2543–2555.

218. Kay ER, Lee J, Nocera DG, Bawendi MG. Angew Chem Int Ed. 2013; 52:1165–1169.

219. Yoshihara T, Yamaguchi Y, Hosaka M, Takeuchi T, Tobita S. Angew Chem Int Ed. 2012; 51:4148–4151.

220. Coogan MP, Court JB, Gray VL, Hayes AJ, Lloyd AH, Millet CO, Pope SJA, Lloyd D. Photochem Photobiol Sci. 2010; 9:103–109. [PubMed: 20062850]

221. Okura, I.; Kamachi, T. Handbook of Porphyrin Science. In: Kadish, KM.; Smith, KM.; Guilard, R., editors. World Scientific Publishing: Singapore. Vol. 12. 2011. p. 297-348.

222. Tripathi VS, Lakshminarayana G, Nogami M. Sens Actuators, B. 2010; 147:741–747.

223. Amao Y, Miyakawa K, Okura I. J Mater Chem. 2000; 10:305–308.

224. Zhang H, Sun Y, Ye K, Zhang P, Wang Y. J Mater Chem. 2005; 15:3181–3186.

225. Jorge PAS, Mayeh M, Benrashid R, Caldas P, Santos JL, Farahi F. Proc SPIE. 2005; 5855:391–394.

226. Jorge PAS, Mayeh M, Benrashid R, Caldas P, Santos JL, Farahi F. Appl Opt. 2006; 45:3760–3767. [PubMed: 16724134]

227. Wang X, Chen X, Xie Z, Wang X. Angew Chem Int Ed. 2008; 47:7450–7453.

228. Collier BB, Singh S, McShane M. Analyst. 2011; 136:962–967. [PubMed: 21170467]

229. Sung TW, Lo YL. Sens Actuators, B. 2012; 173:406–413.

230. Zhang C, Ingram J, Schiff S, Xu J, Xiao M. Proc SPIE. 2011; 7947:79470B/1–6.

231. Ingram JM, Zhang C, Xu J, Schiff SJ. J Neurosci Methods. 2013; 214:45–51. [PubMed: 23333398]

232. Amelia M, Lavie-Cambot A, McClenaghan ND, Credi A. Chem Commun. 2011; 47:325–327.

233. McLaurin EJ, Greytak AB, Bawendi MG, Nocera DG. J Am Chem Soc. 2009; 131:12994–13001. [PubMed: 19697933]

234. Stern O, Volmer M. Z Phys. 1919; 20:183–188.

235. Lemon CM, Karnas E, Bawendi MG, Nocera DG. Inorg Chem. submitted for publication.

236. Fleming ID, Pegler HF. Analyst. 1963; 88:967–968.

237. Robyt, JF.; White, BJ. Biochemical Techniques: Theory and Practice. Waveland Press; Prospect Heights, IL: 1990. p. 220-221.

238. Cao L, Ye J, Tong L, Tang B. Chem Eur J. 2008; 14:9633–9640. [PubMed: 18792902]

239. Yuan J, Guo W, Yin J, Wang E. Talanta. 2009; 77:1858–1863. [PubMed: 19159810]

240. Hu M, Tian J, Lu HT, Weng LX, Wang LH. Talanta. 2010; 82:997–1002. [PubMed: 20678658]

241. Wu P, He Y, Wang HF, Yan XP. Anal Chem. 2010; 82:1427–1433. [PubMed: 20092317]

242. Saran AD, Sadawana MM, Srivastava R, Bellare JR. Colloids Surf A. 2011; 384:393–400.

243. Mansur A, Mansur H, González J. Sensors. 2011; 11:9951–9972. [PubMed: 22163736]

244. Yi Y, Deng J, Zhang Y, Li H, Yao S. Chem Commun. 2013; 49:612–614.

245. Li X, Zhou Y, Zheng Z, Yue X, Dai Z, Liu S, Tang Z. Langmuir. 2009; 25:6580–6586. [PubMed: 19260661]

246. Wang X, Chen H, Zhou T, Lin Z, Zheng J, Xie Z, Chen X, Wong K, Chen G, Wang X. Biosens Bioelectron. 2009; 24:3702–3705. [PubMed: 19523808]

247. Jang E, Kim S, Koh W. Biosens Bioelectron. 2012; 31:529–536. [PubMed: 22177543]

248. Liu Q, Lu X, Li J, Yao X, Li J. Biosens Bioelectron. 2007; 22:3203–3209. [PubMed: 17416515]

249. Cavaliere-Jaricot S, Darbandi M, Kuçur E, Nann T. Microchim Acta. 2008; 160:375–383.

250. Zheng M, Cui Y, Li X, Liu S, Tang Z. J Electroanal Chem. 2011; 656:167–173.

251. Tanne J, Schäfer D, Khalid W, Parak WJ, Lisdat F. Anal Chem. 2011; 83:7778–7785. [PubMed: 21870859]

252. Wang W, Bao L, Lei J, Tu W, Ju H. Anal Chim Acta. 2012; 744:33–38. [PubMed: 22935371]

253. Alvi NH, Soto Rodriguez PDE, Gómez VJ, Kumar P, Amin G, Nur O, Willander M, Nötzel R. Appl Phys Lett. 2012; 101:153110/1–4.

254. Cheng L, Deng S, Lei J, Ju X. Analyst. 2012; 137:140–144. [PubMed: 22034620]

255. Bahshi L, Freeman R, Gill R, Willner I. Small. 2009; 5:676–680. [PubMed: 19226598]

256. Duong HD, Rhee JI. Talanta. 2007; 73:899–905. [PubMed: 19073118]

257. Yuan J, Guo W, Wang E. Biosens Bioelectron. 2008; 23:1567–1571. [PubMed: 18356038]

258. Saa L, Pavlov V. Small. 2012; 8:3449–3455.

259. Pan H, Cui R, Zhu JJ. J Phys Chem B. 2008; 112:16895–16901. [PubMed: 19367897]

260. Medintz IL, Clapp AR, Mattoussi H, Goldman ER, Fisher B, Mauro JM. Nat Mater. 2003; 2:630–638. [PubMed: 12942071]

261. Hu B, Zhang LP, Chen ML, Chen ML, Wang JH. Biosens Bioelectron. 2012; 32:82–88. [PubMed: 22192453]

262. Tang B, Cao L, Xu K, Zhou L, Ge J, Li Q, Yu L. Chem Eur J. 2008; 14:3637–3644. [PubMed: 18318025]

263. Liao KC, Hogen-Esch T, Richmond FJ, Marcu L, Loeb GE. Proc SPIE. 2005; 5691:129–145.

264. Liao KC, Hogen-Esch T, Richmond FJ, Marcu L, Clifton W, Loeb GE. Proc SPIE. 2006; 6083:60830V/1–9.

265. Liao KC, Hogen-Esch T, Richmond FJ, Marcu L, Clifton W, Loeb GE. Biosens Bioelectron. 2008; 23:1458–1465. [PubMed: 18304798]

266. Wu W, Zhou T, Berliner A, Banerjee P, Zhou S. Angew Chem Int Ed. 2010; 49:6554–6558.

267. Wu W, Zhou T, Shen J, Zhou S. Chem Commun. 2009:4390–4392.

268. Wu W, Zhou T, Aiello M, Zhou S. Proc SPIE. 2010; 7575:75750F/1–6.

269. Cordes DB, Gamsey S, Singaram B. Angew Chem Int Ed. 2006; 45:3829–3832.

270. Feng L, Wang Y, Liang F, Wang X, Zhang L. Sens Actuators, B. 2011; 156:499–503.

271. Cordes DB, Singaram B. Pure Appl Chem. 2012; 84:2183–2202.

272. Yoon J, Czarnik AW. J Am Chem Soc. 1992; 114:5874–5875.

273. James TD, Sandanayake KRAS, Shinkai S. J Chem Soc Chem Commun. 1994:477–478.

274. James TD, Sandanayake KRAS, Shinkai S. Angew Chem Int Ed Engl. 1994; 33:2207–2209.

275. James TD, Sandanayake KRAS, Iguchi R, Shinkai S. J Am Chem Soc. 1995; 117:8982–8987.

276. Ni W, Kaur G, Springsteen G, Wang B, Franzen S. Bioorg Chem. 2004; 32:571–581. [PubMed: 15530997]

277. de Silva A, Moody TS, Wright GD. Analyst. 2009; 134:2385–2393. [PubMed: 19918605]

278. Kawanishi T, Romey MA, Zhu PC, Holody MZ, Shinkai S. J Fluoresc. 2004; 14:499–512. [PubMed: 15617258]

279. Sletten EM, Bertozzi CR. Angew Chem Int Ed. 2009; 48:6974–6998.

280. Devaraj NK, Weissleder R, Hilderbrand SA. Bioconjugate Chem. 2008; 19:2297–2299.

281. Devaraj NK, Hilderbrand S, Upadhyay R, Mazitschek R, Weissleder R. Angew Chem Int Ed. 2010; 49:2869–2872.

282. Han HS, Devaraj NK, Lee J, Hilderbrand SA, Weissleder R, Bawendi MG. J Am Chem Soc. 2010; 132:7838–7839. [PubMed: 20481508]

283. Smith AM, Duan H, Mohs AM, Nie S. Adv Drug Delivery Rev. 2008; 60:1226–1240.

284. Biju V, Mundayoor S, Omkumar RV, Anas A, Ishikawa M. Biotechnol Adv. 2010; 28:199–213. [PubMed: 19969062]

285. Berlman, IB. Handbook of Fluorescence Spectra of Aromatic Molecules. Academic Press; New York: 1971.

286. Yuan F, Salehi HA, Boucher Y, Vasthare US, Tuma RF, Jain RK. Cancer Res. 1994; 54:4564–4568. [PubMed: 8062241]

287. Leunig M, Yuan F, Menger MD, Boucher Y, Goetz AE, Messmer K, Jain RK. Cancer Res. 1992; 52:6553–6560. [PubMed: 1384965]
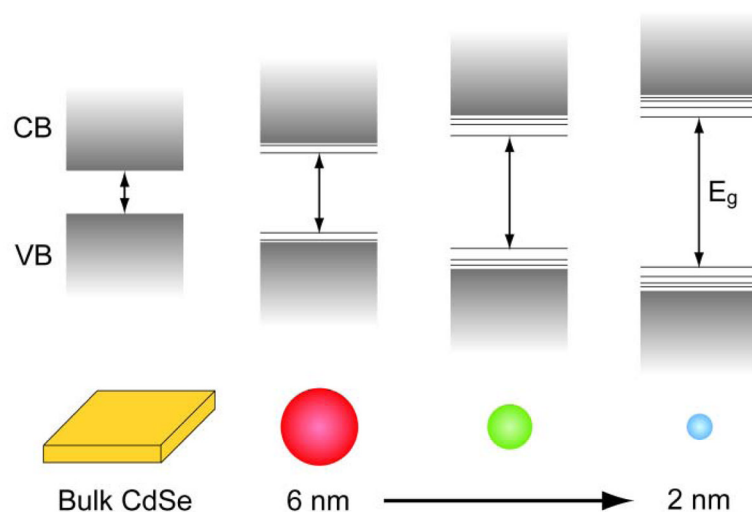
Figure 1.
Schematic of quantum confinement. As the size of the particle decreases, the exciton or bound electron-hole pair is confined to the dimension of the particle and behaves like a particle in a box with $E \sim 1/r^2$. This results in an increase in the effective band gap (E_g) of the semiconductor and the formation of discrete energy levels at the band edges.
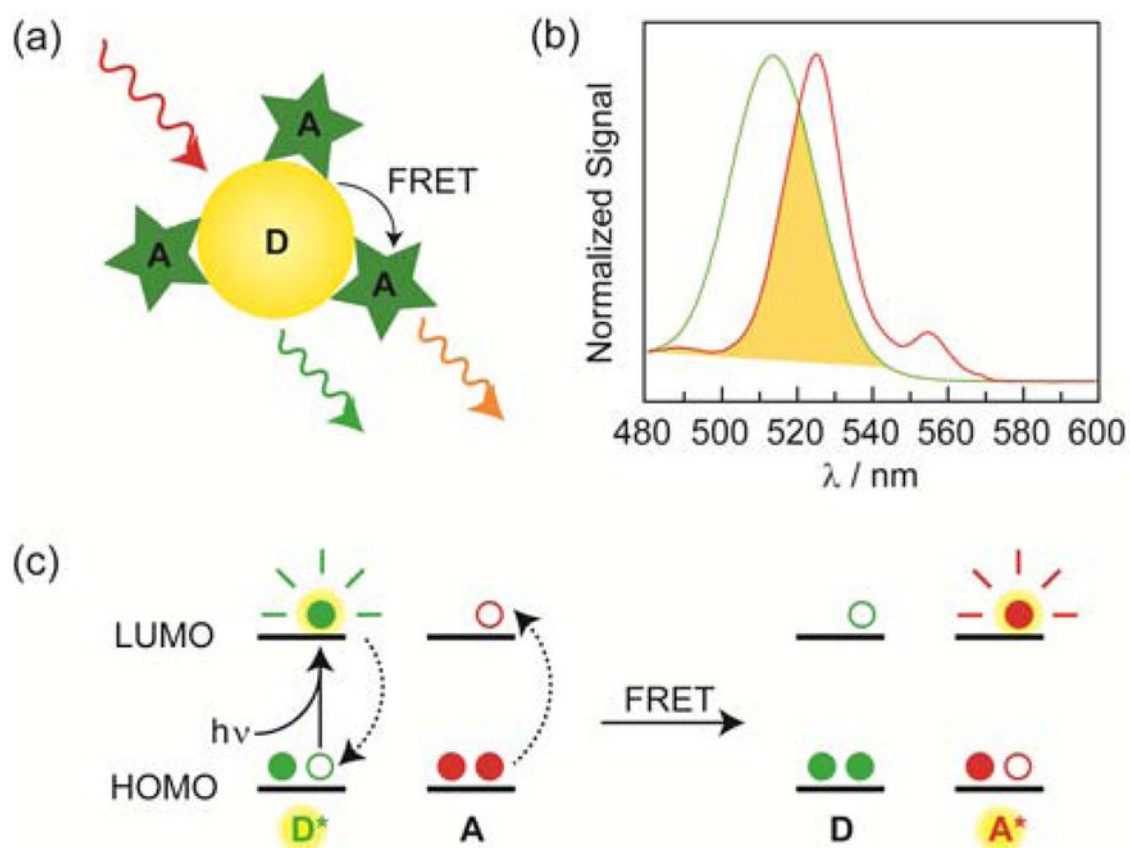
Figure 2.
(a) Schematic representation of a QD donor (D) and fluorophore acceptor (A), which is promoted to an excited electronic state via FRET. (b) Illustration of spectral overlap between donor emission (—) and acceptor absorption (—) profiles. (c) Molecular orbital representation of the FRET process.
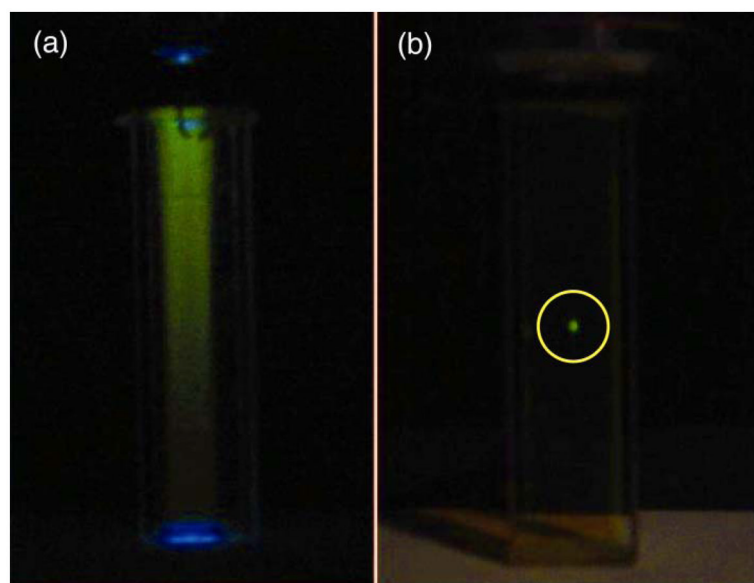
Figure 3.
(a) One-photon and (b) two-photon excitation of the same sample of fluorescein. Two-photon excitation produces fluorescence within the focal volume, which is highlighted with a yellow circle.
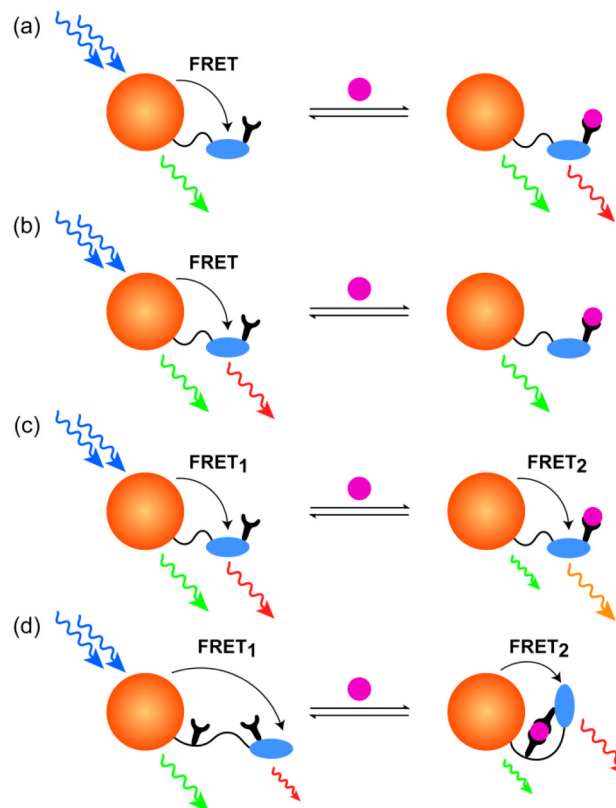
Figure 4.
Schematic representation of the optical responses utilized in our sensors. (a) A turn-on sensor exhibits fluorescence enhancement upon analyte binding. (b) A turn-off sensor exhibits fluorescence quenching in the presence of analyte. The final two strategies illustrate sensing via changes in FRET efficiency by either modulating the spectral overlap integral (c) or changing the donor-acceptor distance (d) as a function of analyte concentration.
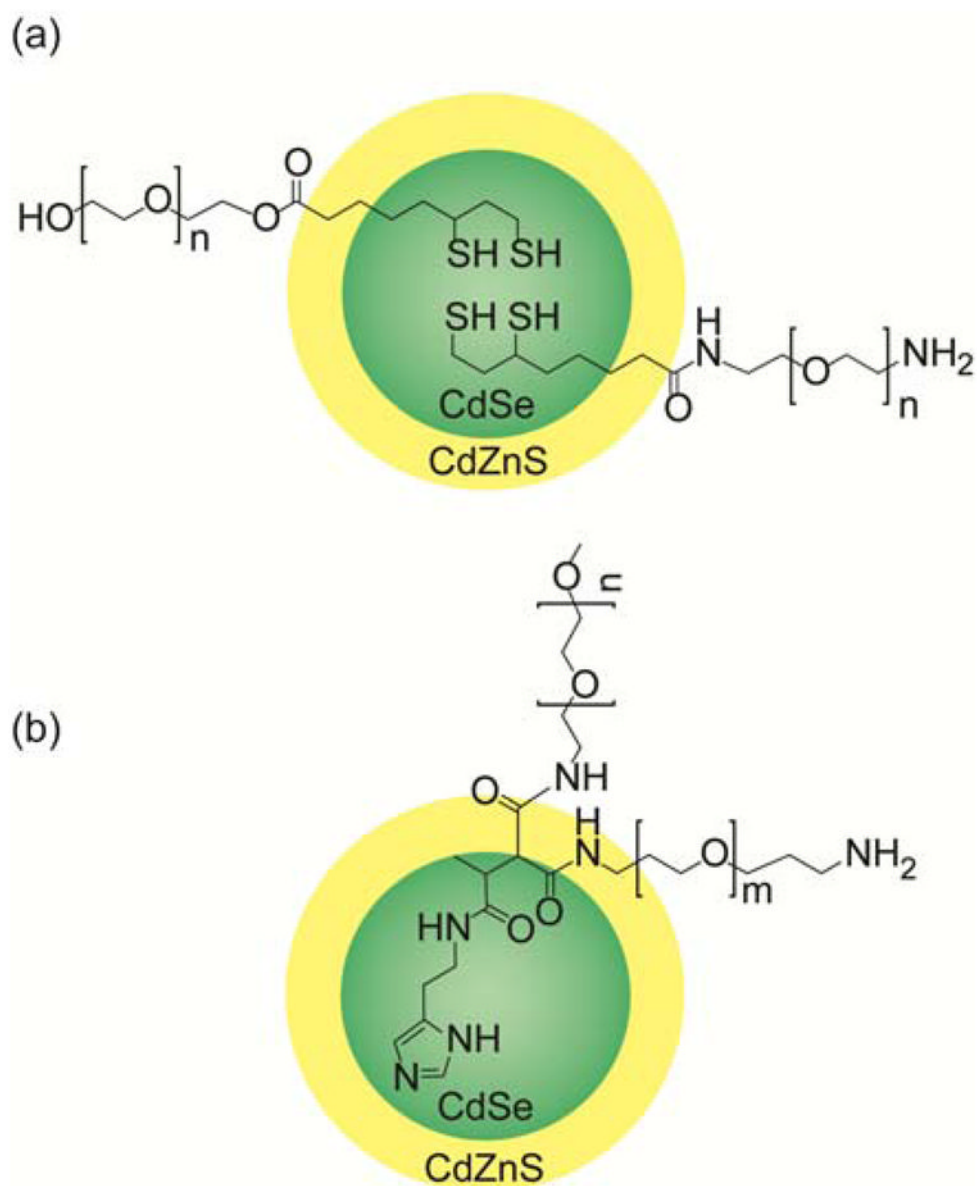
Figure 5.
Schematic representation of hydrophilic ligands developed in our research groups to solubilize QDs: (a) DHLA-PEG and (b) poly(PEG)-PIL. These ligands feature a terminal amine group that enables further derivitization.
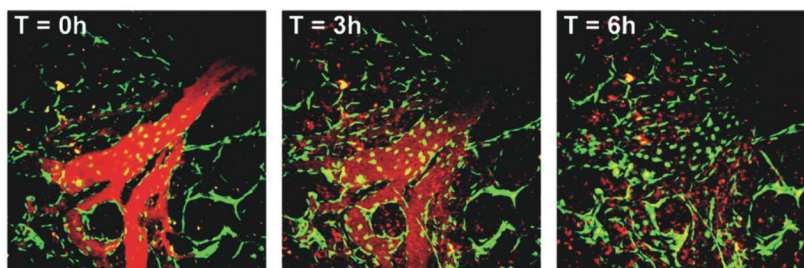
Figure 6.
Time lapse *in vivo* two-photon imaging of a breast cancer tumor in a mouse model, studying the distribution dynamics of PIL-coated QDs. Red signal is due to PIL-QD emission while the green signal is from green fluorescence protein (GFP) expressed on the surface of vascular endothelial cells that line the vessel wall. After injection (t = 0 h), the QD is confined to the vessel. Over time, the QDs extravasate and diffuse into the tumor tissue, giving a homogeneous distribution after 6 hours. Reprinted with permission from Ref. 173. Copyright 2010 American Chemical Society.
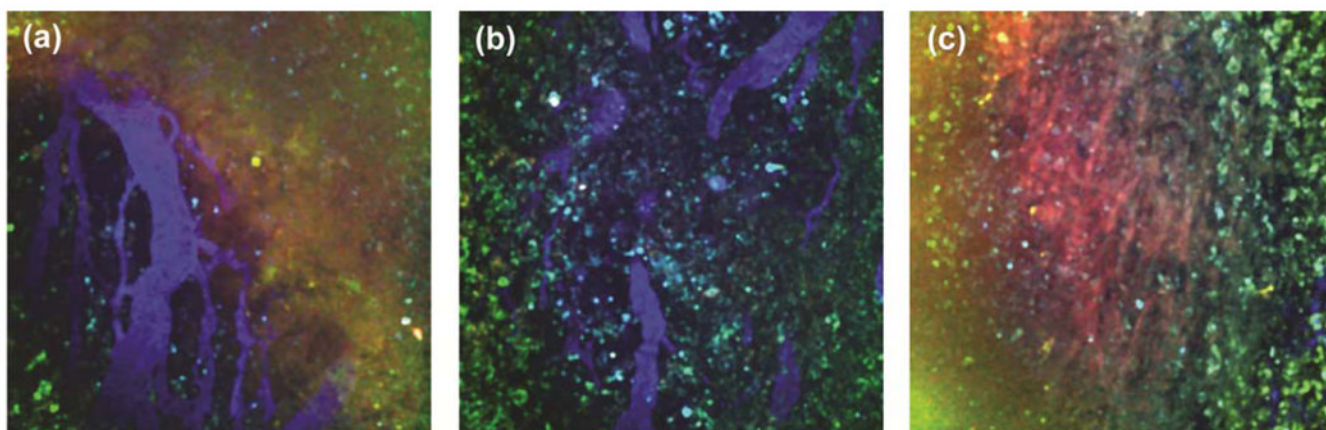
Figure 7.
Preliminary *in vivo* imaging and pH sensing using a QD-SNARF conjugate in a LS174T human colorectal adenocarcinoma model. (a) A highly vascularized area of a tumor clearly demonstrates the distended, irregular nature of tumor blood vessels. (b) An area of the tumor which demonstrates more normalized vasculature, in contrast to the vessels presented in (a). (c) An area of tumor tissue not adjacent to vessels, which is dominated by SNARF and QD emission.
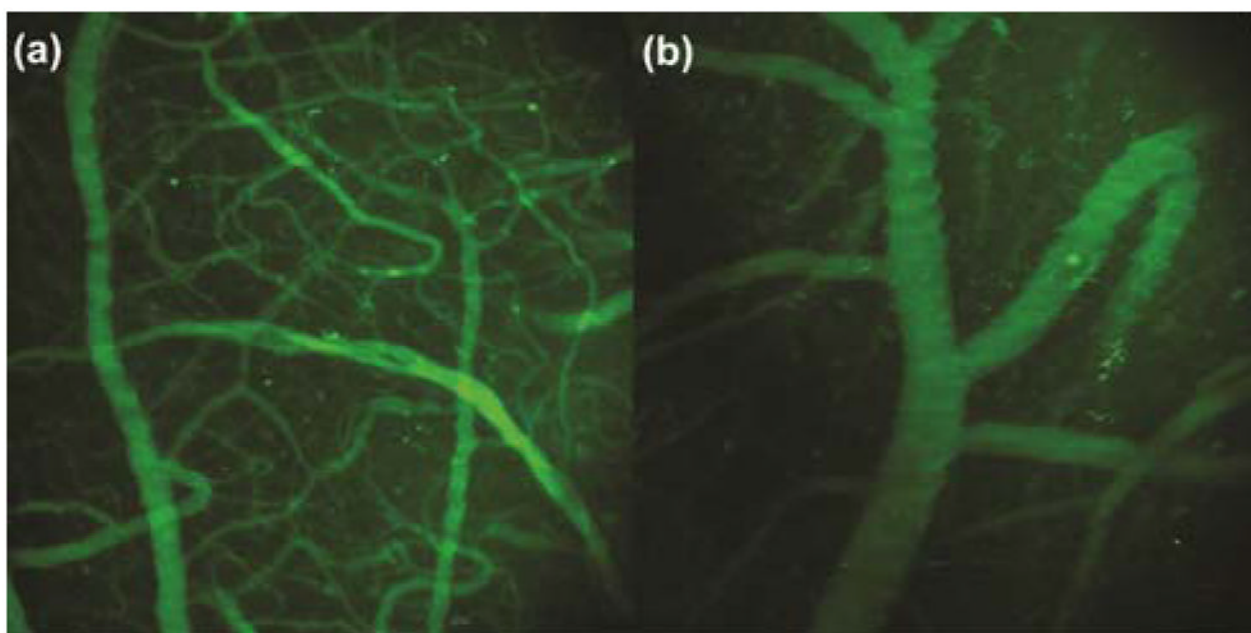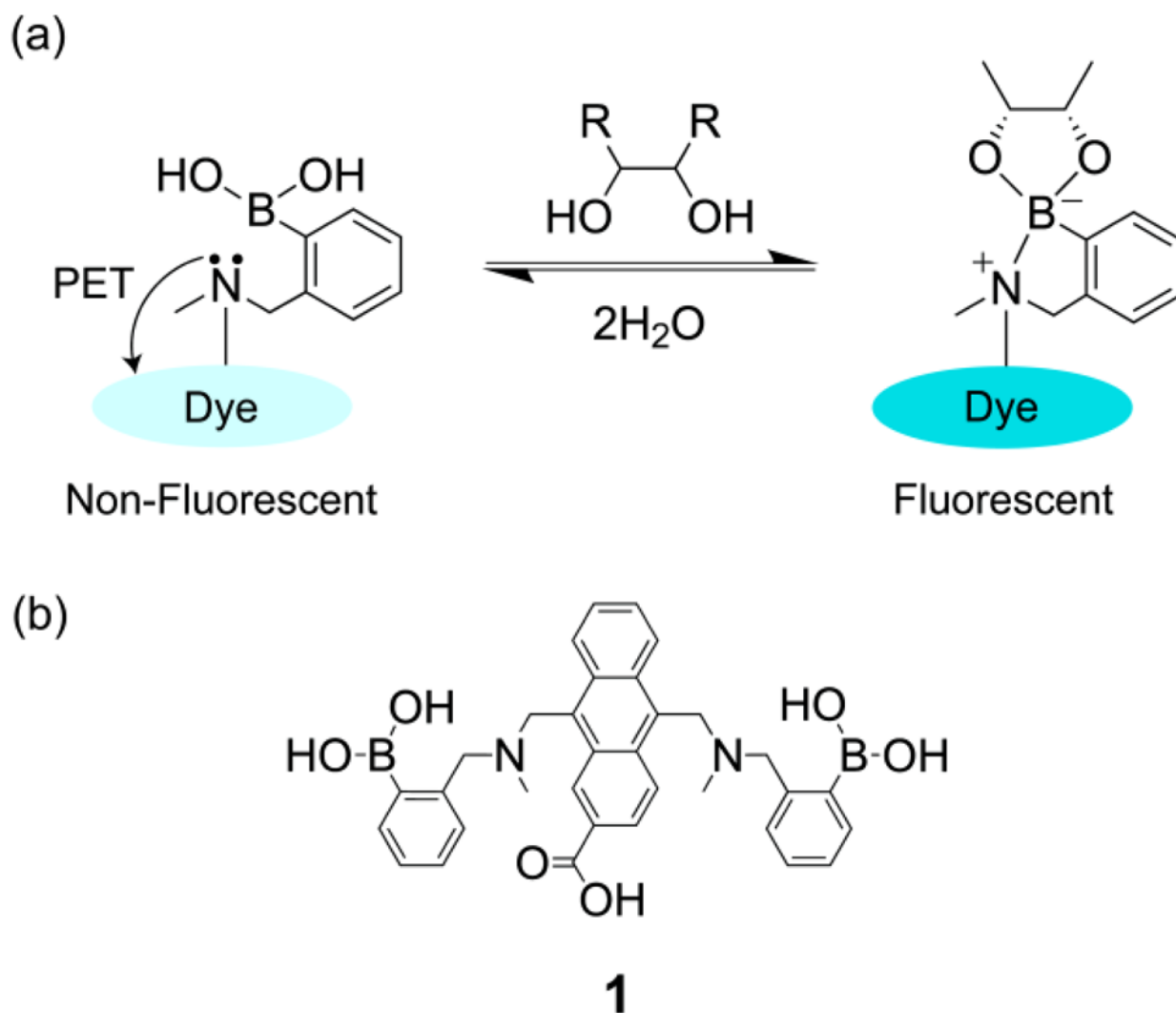
Figure 8.
In vivo images obtained from cranial window imaging with micelle-encapsulated QD:porphyrin conjugates. Both (a) and (b) are three-dimensional depth projections obtained from imaging over a distance of 200 μm in 10 μm steps. The apparent "ridges" in the vessels, particularly noticeable in the large vessels of (b), are due to the mouse breathing.

Figure 9.
(a) Mechanism of glucose sensing using a boronic acid-modified fluorophore. In the absence of glucose, the lone pair of the amine nitrogen quenches the dye fluorescence via PET. When glucose binds to the boronic acid, the strength of the B–N interaction increases, allowing the dye molecule to fluoresce. (b) Molecular structure of the glucose-sensing fluorophore **1** used in this study.
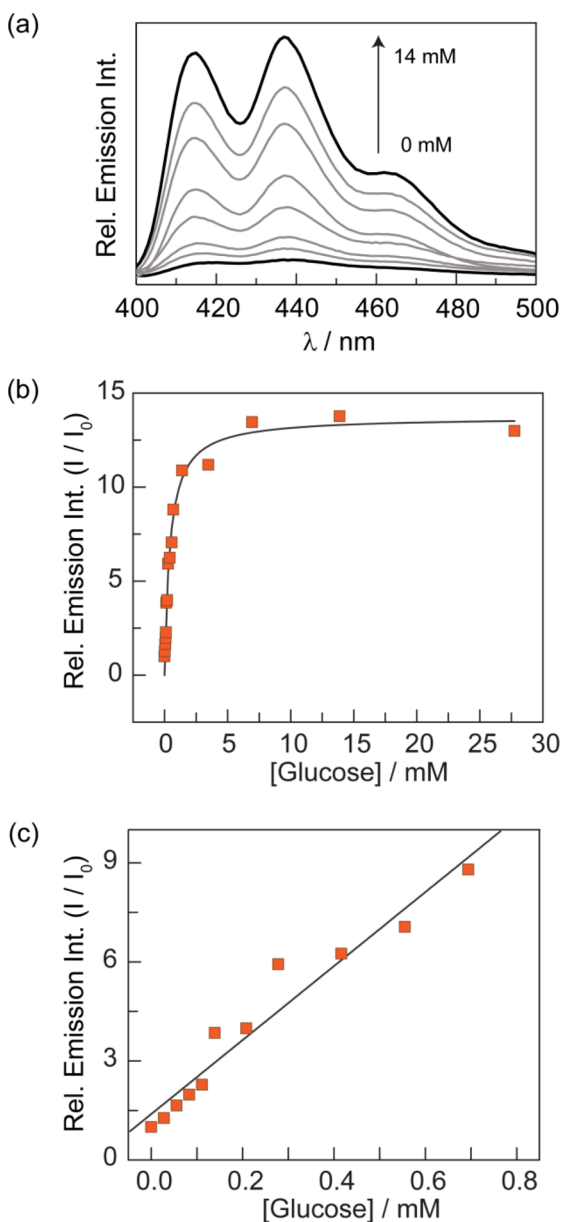
Figure 10.
(a) Emission spectra (λ_{exc} = 384 nm) of **1** as a function of glucose concentration: 0 mM, 0.06 mM, 0.11 mM, 0.21 mM, 0.42 mM, 0.69 mM, 1.39 mM, and 13.88 mM. (b) Plot of normalized emission signal at 437 nm versus glucose concentration, exhibiting saturation above 5 mM glucose. (c) Demonstration of the linear response of **1** at low (< 1 mM) glucose concentration.